

**Field-induced quantum spin disordered state in spin-1/2 honeycomb magnet**  
**Na<sub>2</sub>Co<sub>2</sub>TeO<sub>6</sub>**

Gaoting Lin<sup>1</sup>, Jaehong Jeong<sup>2,3</sup>, Chaebin Kim<sup>2,4</sup>, Yao Wang<sup>5,6</sup>, Qing Huang<sup>7</sup>,  
Takatsugu Masuda<sup>8</sup>, Shinichiro Asai<sup>8</sup>, Shinichi Itoh<sup>9</sup>, Gerrit Günther<sup>10</sup>, Margarita  
Russina<sup>10</sup>, Zhilun Lu<sup>10,11</sup>, Jieming Sheng<sup>12,13,14</sup>, Le Wang<sup>14</sup>, Jiucui Wang<sup>15</sup>, Guohua  
Wang<sup>1</sup>, Qingyong Ren<sup>1,12,13</sup>, Chuanying Xi<sup>16</sup>, Wei Tong<sup>16</sup>, Langsheng Ling<sup>16</sup>,  
Zhengxin Liu<sup>15</sup>, Liusuo Wu<sup>14</sup>, Jiawei Mei<sup>14</sup>, Zhe Qu<sup>16,17</sup>, Haidong Zhou<sup>7</sup>, Xiaoqun  
Wang<sup>1</sup>, Je-Geun Park<sup>2,4</sup>, Yuan Wan<sup>5,6,18,\*</sup>, and Jie Ma<sup>1,\*</sup>

<sup>1</sup>*Key Laboratory of Artificial Structures and Quantum Control, Shenyang National  
Laboratory for Materials Science, School of Physics and Astronomy, Shanghai Jiao  
Tong University, Shanghai 200240, China*

<sup>2</sup>*Department of Physics and Astronomy, Seoul National University, Seoul 08826,  
Republic of Korea*

<sup>3</sup>*Center for Correlated Electron Sciences, Institute for Basic Science (IBS), Seoul  
08826, Republic of Korea*

<sup>4</sup>*Center for Quantum Materials, Seoul National University, Seoul 08826, Republic of  
Korea*

<sup>5</sup>*Institute of Physics, Chinese Academy of Sciences, Beijing 100190, China*

<sup>6</sup>*University of Chinese Academy of Sciences, Beijing 100049, China*

<sup>7</sup>*Department of Physics and Astronomy, University of Tennessee, Knoxville, Tennessee  
37996, USA*

<sup>8</sup>*Institute for Solid State Physics, University of Tokyo, Kashiwanoha, Kashiwa, Chiba  
277-8581, Japan*

<sup>9</sup>*Institute of Materials Structure Science, High Energy Accelerator Research  
Organization, Tsukuba 305-0801, Japan*

<sup>10</sup>*Helmholtz-Zentrum Berlin für Materialien und Energie, Hahn-Meitner-Platz 1,  
Berlin 14109, Germany*

<sup>11</sup>*The Henry Royce Institute and Department of Materials Science and Engineering,  
The University of Sheffield, Sir Robert Hadfield Building, Sheffield, S1 3JD, United*

*Kingdom*

<sup>12</sup>*Spallation Neutron Source Science Center, Dongguan 523803, China*

<sup>13</sup>*Institute of High Energy Physics, Chinese Academy of Sciences, Beijing 100049,  
China*

<sup>14</sup>*Shenzhen Institute for Quantum Science and Engineering (SIQSE) and Department  
of Physics, Southern University of Science and Technology (SUSTech), Shenzhen,  
Guangdong 518055, China*

<sup>15</sup>*Department of Physics, Renmin University of China, Beijing 100872, China*

<sup>16</sup>*Anhui Province Key Laboratory of Condensed Matter Physics at Extreme  
Conditions, High Magnetic Field Laboratory, Hefei Institutes of Physical Sciences,  
Chinese Academy of Science, Hefei, Anhui 230031, China*

<sup>17</sup>*CAS Key Laboratory of Photovoltaic and Energy Conservation Materials, Hefei  
Institutes of Physical Sciences, Chinese Academy of Sciences, Hefei, Anhui 230031,  
China*

<sup>18</sup>*Songshan Lake Materials Laboratory, Dongguan, Guangdong 523808, China*

\*Corresponding author: [yuan.wan@iphy.ac.cn](mailto:yuan.wan@iphy.ac.cn)

[jma3@sjtu.edu.cn](mailto:jma3@sjtu.edu.cn)

## Abstract

Spin-orbit coupled honeycomb magnets with the Kitaev interaction have received a lot of attention due to their potential of hosting exotic quantum states including quantum spin liquids. Thus far, the most studied Kitaev systems are  $4d/5d$ -based honeycomb magnets. Recent theoretical studies predicted that  $3d$ -based honeycomb magnets, including  $\text{Na}_2\text{Co}_2\text{TeO}_6$  (NCTO), could also be a potential Kitaev system. Here, we have used a combination of heat capacity, magnetization, electron spin resonance measurements alongside inelastic neutron scattering (INS) to study NCTO's quantum magnetism, and we have found a field-induced spin disordered state in an applied magnetic field range of  $7.5 \text{ T} < \mathbf{B} (\perp b\text{-axis}) < 10.5 \text{ T}$ . The INS spectra were also simulated to tentatively extract the exchange interactions. As a  $3d$ -magnet with a field-induced disordered state on an effective spin-1/2 honeycomb lattice, NCTO expands the Kitaev model to  $3d$  compounds, promoting further interests on the spin-orbital effect in quantum magnets.

## INTRODUCTION

Magnets with significant spin-orbital couplings (SOCs) have become a new playground for quantum magnetism in recent years thanks to their potential of hosting novel quantum phases of matter<sup>1</sup>. A prominent example is the Kitaev model, an exactly solvable spin model that features a topological quantum spin liquid (QSL) ground state<sup>2-5</sup>. Microscopically, such a model could emerge from magnetic insulators with competing, spin anisotropic exchange interactions<sup>3</sup>. The essential prerequisites are that (a) the magnetic ions have spin-orbital entangled, Kramers degenerate ground states and (b) they are arranged on a suitable lattice, with the two-dimensional (2D) honeycomb lattice being the simplest example<sup>2-5</sup>. So far, the search for the material incarnations of the Kitaev model has been focused on  $4d/5d$  transition metal based systems due to their relatively strong SOC<sup>4,5</sup>. The examples include  $\text{H}_3\text{LiIr}_2\text{O}_6$ ,  $\alpha\text{-Li}_2\text{IrO}_3$ ,  $\alpha\text{-Na}_2\text{IrO}_3$ , and  $\alpha\text{-RuCl}_3$ <sup>4-15</sup>.  $\text{H}_3\text{LiIr}_2\text{O}_6$  was initially thought to be a QSL, but later studies argue for a random singlet state resulted from the quenched disorder induced by the mobile protons<sup>6,7</sup>. As for  $\alpha\text{-Li}_2\text{IrO}_3$ ,  $\alpha\text{-Na}_2\text{IrO}_3$ , and  $\alpha\text{-RuCl}_3$ , all of them magnetically order due to the non-Kitaev interactions<sup>8-15</sup>. To describe these materials, the Kitaev model has been extended to a generalized Heisenberg-Kitaev (H-K) model with five symmetry-allowed terms, Kitaev term  $K$ , off-diagonal symmetric exchange term  $\Gamma$  and  $\Gamma'$ , nearest-neighbor (NN) Heisenberg coupling  $J$ , and the third NN Heisenberg coupling  $J_3$ <sup>8-24</sup>.  $\alpha\text{-RuCl}_3$  is unique among these materials in that its effective Hamiltonian features a dominant Kitaev term<sup>12,15,19-21</sup>. Remarkably, applying an in-plane magnetic field around 7 T greatly suppresses its magnetic order and induces a potential QSL state<sup>23,25-34</sup>.

More recently, the theoretical studies suggest that Kitaev physics could also be found in honeycomb magnets made of cobalt, a  $3d$  transition metal<sup>35-37</sup>. In  $3d^7$  Co ( $t_{2g}^5 e_g^2$ ) compounds, the spin-active  $e_g$  electrons not only generate new spin-orbit exchange channels of  $t_{2g}\text{-}e_g$  and  $e_g\text{-}e_g$  in addition to the  $t_{2g}\text{-}t_{2g}$  channel operating in  $d^5$  systems with  $t_{2g}$ -only electrons but also produce the Kitaev interaction almost entirely from the  $t_{2g}\text{-}e_g$  process<sup>37</sup>. Moreover, the  $t_{2g}\text{-}e_g$  and  $e_g\text{-}e_g$  contributions to  $\Gamma$  and  $\Gamma'$  are of

opposite signs and largely cancel each other <sup>37</sup>. This makes the cobaltates good candidates for realizing the Kitaev model <sup>35-37</sup>. A pertinent material is the honeycomb magnet  $\text{Na}_2\text{Co}_2\text{TeO}_6$  (NCTO) <sup>35-37</sup>. The other example we are aware of is  $\text{BaCo}_2(\text{AsO}_4)_2$ , which also shows a similar field-induced disordered state at low magnetic field <sup>38</sup>.

As we shall present below, our studies show that NCTO fulfills all the prerequisites for Kitaev physics despite its seeming differences from the preceding  $4d/5d$  compounds. Furthermore, we observe a QSL-like spin disordered state in an applied magnetic field  $\mathbf{B} \perp b$ -axis (parallel to Co-Co bond) and  $7.5 \text{ T} < \mathbf{B} < 10.5 \text{ T}$ . This result suggests NCTO could be a novel honeycomb magnet that exhibits a field-induced disordered state and may broaden our horizon in the quest for Kitaev materials.

## RESULTS

**Specific heat and magnetic susceptibility.** The magnetic specific heat at 0 T measured on polycrystalline sample shows a sharp peak at  $T_N = 25 \text{ K}$ , and its derivative shows another two anomalies at  $T_F = 15 \text{ K}$  and  $T^* = 7 \text{ K}$ , Fig. 1a. Their values are consistent with the previous reports <sup>39-44</sup>. With an increasing magnetic field, the sharp peak at  $T_N$  shifts to lower temperatures and becomes broader. Eventually, it is indiscernible above  $7.5 \text{ T}$  <sup>44</sup>, which indicates that the magnetic ordering at  $T_N$  has been suppressed, and the system enters a magnetically disordered state. Supplementary Fig. 2 presents the heat capacity as a function of temperature at various fields, and the coincident heat capacity suggests no missing entropy above 50 K. The magnetic entropy  $S_{\text{mag}}$  is obtained after subtracting the lattice contribution calculated by the Debye-Einstein (DE) model using Supplementary S(1) (Supplementary Fig. 2). Integrating  $C_{\text{mag}}/T$  over temperature from 100 Kelvin down to 2 Kelvin yields the residual magnetic entropy  $S_{\text{mag}}(0 \text{ T}) = 3.05 \text{ J}/(\text{mol} \cdot \text{K})$ , which is about 27% of the theoretical total magnetic entropy, Fig. 1b. Remarkably, the residual entropy increases with increasing fields in NCTO. This unusual behavior may be contrasted with other magnets that are known to possess finite residual magnetic entropy, where the magnetic field tends to reduce the residual entropy rather than enhance it <sup>45-48</sup>.

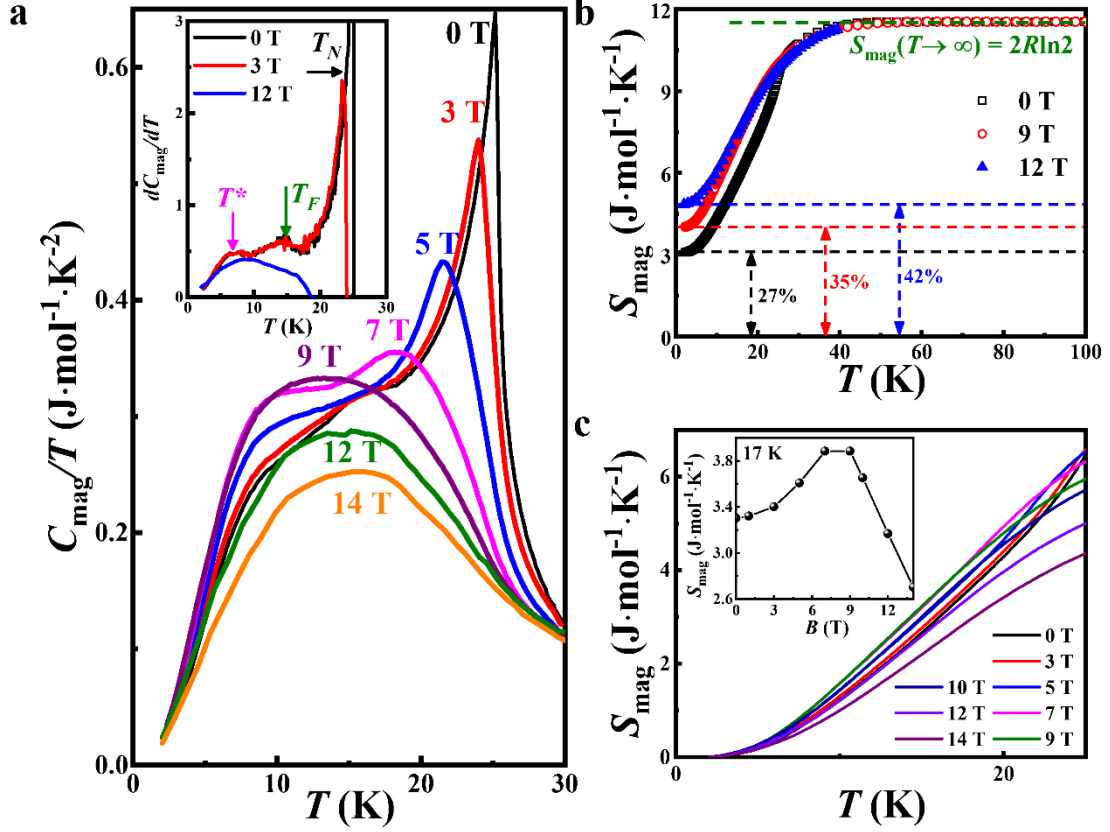


**Fig. 1 Heat capacity of  $\text{Na}_2\text{Co}_2\text{TeO}_6$ .** **a** Temperature dependence of the magnetic specific heat of NCTO for different magnetic fields up to 14 T. The inset shows the differential magnetic specific heat  $dC_{\text{mag}}/dT$ , and three transitions are observed as  $T_N$ ,  $T_F$ , and  $T^*$ , respectively; **b** The magnetic entropy  $S_{\text{mag}}(T)$  at 0 T, 9 T, and 12 T. The olive dashed line refers to  $S_{\text{mag}}(T \rightarrow \infty)$  calculated with effective spin  $J_{\text{eff}} = 1/2$  for  $\text{Co}^{2+}$ . In order to better observe the residual magnetic entropy, the  $S_{\text{mag}}(T)$  curves are shifted vertically so that their maxima coincide with the  $S_{\text{mag}}(T \rightarrow \infty)$ . The black, red, and blue dashed line refers to the possible residual magnetic entropy below 2 K under different magnetic field. Compared with the total magnetic entropy  $S_{\text{mag}}(T \rightarrow \infty)$ , the percentage of residual magnetic entropy in different magnetic fields is shown in the figure; **c** A zoom-in of magnetic entropy below  $T_N$  at various magnetic fields. Note the data are not shifted vertically as opposed to **b**. The inset shows the field dependence of the  $S_{\text{mag}}$  at 17 K.

Another noteworthy feature is that the field dependence of the  $S_{\text{mag}}$  at 17 K (the inset of Fig. 1c), reaches a maximum near 9 T. This non-monotonic behavior of  $S_{\text{mag}}$  with increasing fields mirrors that of the magnetic specific heat  $C_{\text{mag}}/T$  (Fig. 1a), which suggests the energy gap of the magnetic excitations closes at first and then reopens with increasing fields. It is worth mentioned that this field-dependent non-monotonic behavior was also observed in the  $\alpha\text{-RuCl}_3$  as considered a signal of entering the field-induced non-Abelian QSL state<sup>25,27,29</sup>.

Figure 2 shows the DC magnetic susceptibility  $\chi(T)$  measured by the zero-field

cooling process on a single crystalline sample with  $\mathbf{B} \perp b$ -axis in the  $ab$  plane. In low fields, three anomalies at  $T_N$ ,  $T_F$ , and  $T^*$  are observed as shown in Fig. 2a, which mirror the specific heat anomalies. With increasing fields, the peak with the antiferromagnetic (AFM) characteristics at  $T_N$  shifts to lower temperatures and becomes flattened, and the other two anomalies become weaker, Fig. 2b. With  $\mathbf{B} > 7.5$  T, all anomalies are indiscernible. This is consistent with the disappearance of the specific heat peak with  $\mathbf{B} > 7.5$  T and suggests that the system enters a disordered phase.

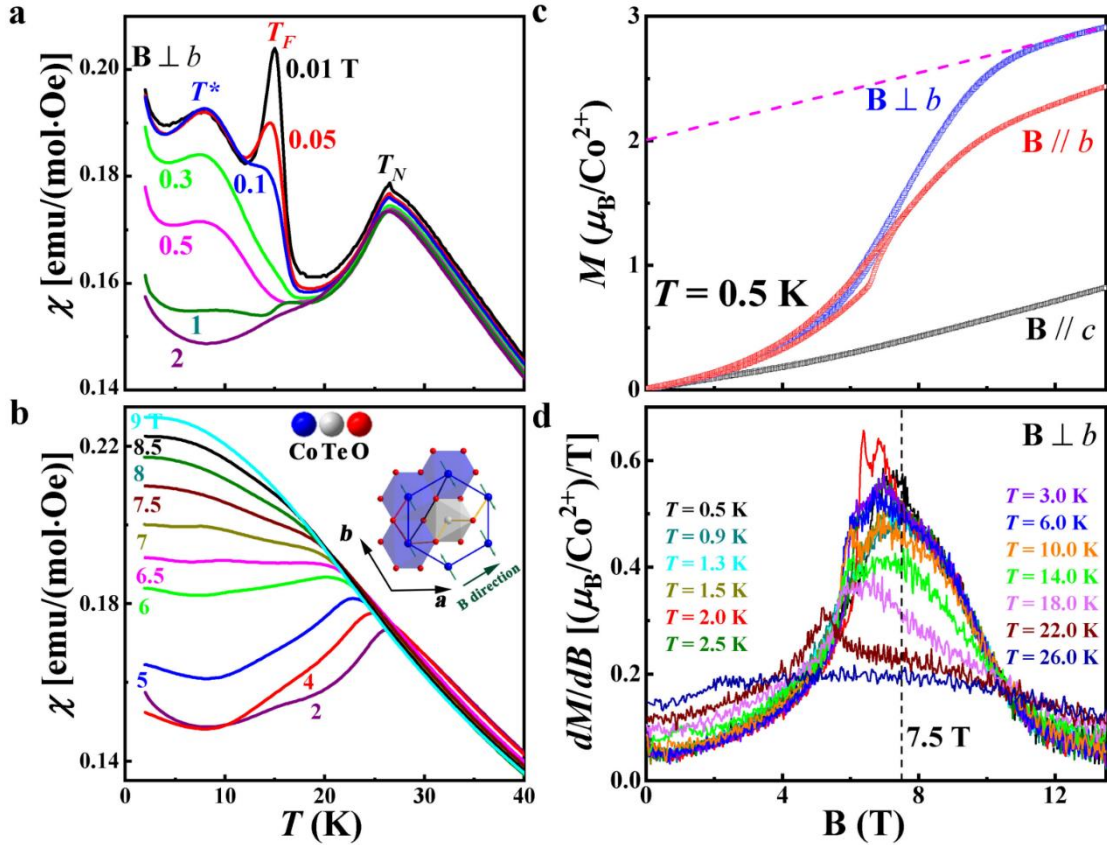


**Fig. 2 Magnetic susceptibility of  $\text{Na}_2\text{Co}_2\text{TeO}_6$  for  $\mathbf{B} \perp b$ -axis.** **a** and **b** Temperature dependence of susceptibility  $\chi(T)$  in NCTO measured at various magnetic fields. The inset of Fig. 2**b** shows the honeycomb lattices of Co viewed along the  $c$  axis. The cartoon shows the moments to be in the basal plane and parallel to  $b$  axis<sup>40,41</sup>, and the  $\text{TeO}_6$  octahedra sit at the center of each honeycomb unit. The first NN ferromagnetic (FM) interaction  $J$  originated from a collaboration between Co-O-Co (red bond) superexchange interactions and Co-Co (blue bond) direct exchange interactions. The second NN  $J_2$  has multiple superexchange interaction pathways, which may lead to a wide range of variations, mainly determined by  $J$  and  $J_3$ . The third NN AFM interaction  $J_3$  arises from the existence of Te atom in the center of honeycomb lattice, which leads to the unique superexchange interaction pathway Co-O-Te-O-Co (golden bond). The olive arrow refers to the direction of applied magnetic field  $\mathbf{B}$  in the magnetization; **c** The isothermal magnetization  $M(\mathbf{B})$  with the applied magnetic field  $\mathbf{B} \perp b$ ,  $\mathbf{B} // b$  and  $\mathbf{B} // c$  axis at 0.5 K, respectively. The dashed line indicates the Van-Vleck paramagnetic background. **d** The differential isothermal magnetization as functions of fields

$dM/dB$  vs.  $\mathbf{B}$  at different temperatures with  $\mathbf{B} \perp b$ .

The magnetization ( $M$ ) measured at 0.5 K with  $\mathbf{B} \perp b$ -axis shows an anomaly around 6 T (Fig. 2c), which leads to a peak on the  $dM/dB$  curve (Fig. 2d). The peak shifts to lower field and becomes weaker with increasing temperature. Above 7.5 T, the  $dM/dB$  data show two opposing temperature-dependent behaviors: the intensity of the  $dM/dB$  decreases with increasing temperature below 10.5 T, whereas it increases with temperature above 10.5 T. The  $dM/dB$  curves at different temperatures all cross approximately at 10.5 T. We also note that for temperatures below 6 K and  $7.5 \text{ T} < \mathbf{B} < 10.5 \text{ T}$ , when the system is in the disordered state as suggested by the specific heat and susceptibility data, the  $dM/dB$  curves qualitatively coincide with each other.

We interpret our magnetization data heuristically as follows<sup>18</sup>. Between 7.5 T and 10.5 T, the system is in a spin-disordered state with short-range spin correlations. On the one hand, the short-range spin correlations increase the  $dM/dB$  intensity with increasing temperatures since these thermal fluctuations thermally activate the spins that can be flipped by the magnetic field. On the other hand, the increasing temperature thermalizes the already polarized spins to decrease the  $dM/dB$  intensity. Therefore, the temperature-independent  $dM/dB$  intensity below 6 K and  $7.5 \text{ T} < \mathbf{B} < 10.5 \text{ T}$  indicates there exists strong short-range spin correlations for such low temperatures in the spin disordered state. Above 6 K and  $7.5 \text{ T} < \mathbf{B} < 10.5 \text{ T}$ , the thermal fluctuations quickly thermalize the already polarized spins so that the  $dM/dB$  intensity decreases with increasing temperature. By contrast, the system crosses over to the polarized state above 10.5 T. Thus, the temperature-independent  $dM/dB$  intensity at 10.5 T reflects a characteristic field at which these two competing effects compensate each other. We therefore take 10.5 T as the crossover field from the correlated spin-disordered state to the spin polarized state. The magnetization curve further suggests that the saturation field for  $\mathbf{B} \perp b$ -axis case is around  $B_S = 12.5 \text{ T}$  with saturation magnetization  $M_S = 2.01\mu_B/\text{Co}^{2+}$  obtained by subtracting off the Van-Vleck paramagnetic contribution<sup>49</sup>, Fig. 2c.

**High-field electron spin resonance (ESR).** As shown in Fig. 3, the high-field ESR data measured at 2 K exhibits a rich excitation spectrum, in which the modes A,

B, and C were observed in the ordered phase and the mode D was only detected with  $\mathbf{B} > 6$  T. The modes A, B, and C can be described by conventional AFM resonance modes and single-magnon excitations at the  $\Gamma$  point<sup>33,50</sup>, the related intensities become weaker and disappear above  $T_N$  with the increasing temperature (Supplementary Fig. 3). The inset of Fig. 3k shows the electron paramagnetic resonance (EPR) spectra measured at 50 K with 214 GHz. From the resonance fields obtained by Supplementary S(2), the calculated  $g$ -factors are  $g_{ab} = 4.13$  and  $g_c = 2.3$ , respectively. These values are also consistent with the magnetization data. The saturation magnetization  $M_S = 2.01\mu_B/\text{Co}^{2+}$  for  $\mathbf{B} \perp b$ -axis, Fig. 2c, leads to a  $g_J = 4.02$  for the pseudospin-1/2 case. Both the ESR and the magnetization data corroborate the effective spin-1/2 model for  $\text{Co}^{2+}$  ions. The higher energy crystal field levels of  $\text{Co}^{2+}$  are thermally inactive in the temperature range considered in this work. The strongly anisotropic  $g$  factors for  $\text{Co}^{2+}$  ions in the octahedral environment confirm the strong SOC and magnetocrystalline anisotropy, which can usually drive a magnetic insulator to open a spin-wave energy gap. The extracted resonance data from Fig. 3a-j are summarized in the frequency-field diagram shown in Fig. 3k, and the extrapolation of the frequency-field dependences of modes A, B, and C to zero field reveal a gap  $\Delta E \approx 100$  GHz  $\approx 0.4$  meV.

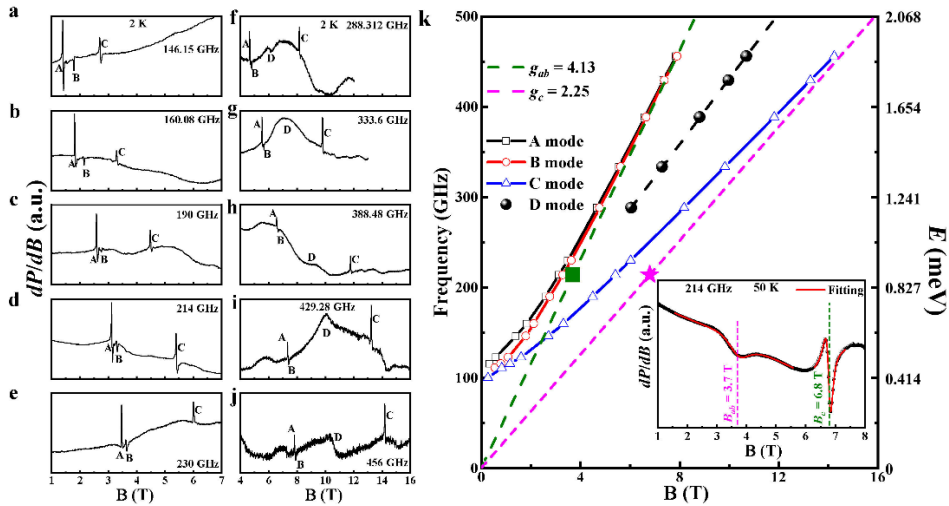


**Fig. 3 High-field ESR of  $\text{Na}_2\text{Co}_2\text{TeO}_6$ .** a-j Frequency-dependence of ESR at 2 K; k ESR frequency-field diagram of NCTO at 2 K. The unit conversion with meV ( $1 \text{ meV} \approx 241.8 \text{ GHz}$ ) is shown in the right axis. The inset shows the EPR spectra measured at 50 K with 214 GHz. The red lines are the fitting line by Supplementary S(2). The olive squares and magenta stars are obtained from the EPR data at 50 K.

Around 7 ~ 8 T, the AFM modes of A and B approach the EPR line with  $g_{ab} = 4.13$ , which again suggests a field-driven magnetically disordered state with paramagnetic-like behavior in the  $ab$ -plane. The field-frequency curves of the A and B modes intersects with EPR line near 6 T, which may be heuristically interpreted as the field at which the spin gap closes. This interpretation is also consistent with the specific heat data, which suggests the gap closes near 6 T. The field-frequency curve of the C mode gradually approaches the EPR line with  $g_c = 2.3$ , which indicates that its polarization is along the  $c$  axis.

The ESR measurement reveals another mode that is not directly connected to the aforementioned AFM resonance modes, which we dub as D mode. It only appears when  $\mathbf{B} > 6$  T. Its excitation energy shows a linear-field dependence with a slope of  $\sim 0.15$  meV/T, from which we deduce an effective  $g \approx 2.6$ . This effective  $g$ -factor is between  $g_{ab}$  and  $g_c$ . The D mode must be associated with a magnetic excitation that only exists or becomes visible in the high-field spin disordered phase. Comparing with the other three modes, the D mode is much weaker, and its linewidth is broader. Its microscopic origin is unclear at the moment; however, we note its close resemblance with the ESR data of  $\alpha$ -RuCl<sub>3</sub>, where new modes with linear field-energy relationship emerge in the spin disordered state<sup>26,28,33</sup>.

**Phase diagram.** A phase diagram was constructed in Fig. 4 by combining the critical temperatures and fields obtained above. There are four regimes: (i) with  $\mathbf{B} < 6$  T, three magnetic transitions occur with decreasing temperatures. The transition at  $T_N$  should be the one from paramagnetic to zigzag AFM ordering. The ones at  $T_F$  and  $T^*$  could be the adjustments of the canting moments of the zigzag order; (ii) For  $6 \text{ T} < \mathbf{B} < 7.5 \text{ T}$ , there is a coexistence of low-field magnetically ordered state and high-field spin disordered state; (iii) Most interestingly, within  $7.5 \text{ T} < \mathbf{B} < 10.5 \text{ T}$ , the system enters a spin disordered state; (iv) With  $\mathbf{B} > 10.5 \text{ T}$ , the system begins to enter the polarized state and becomes fully saturated above 12.5 T.

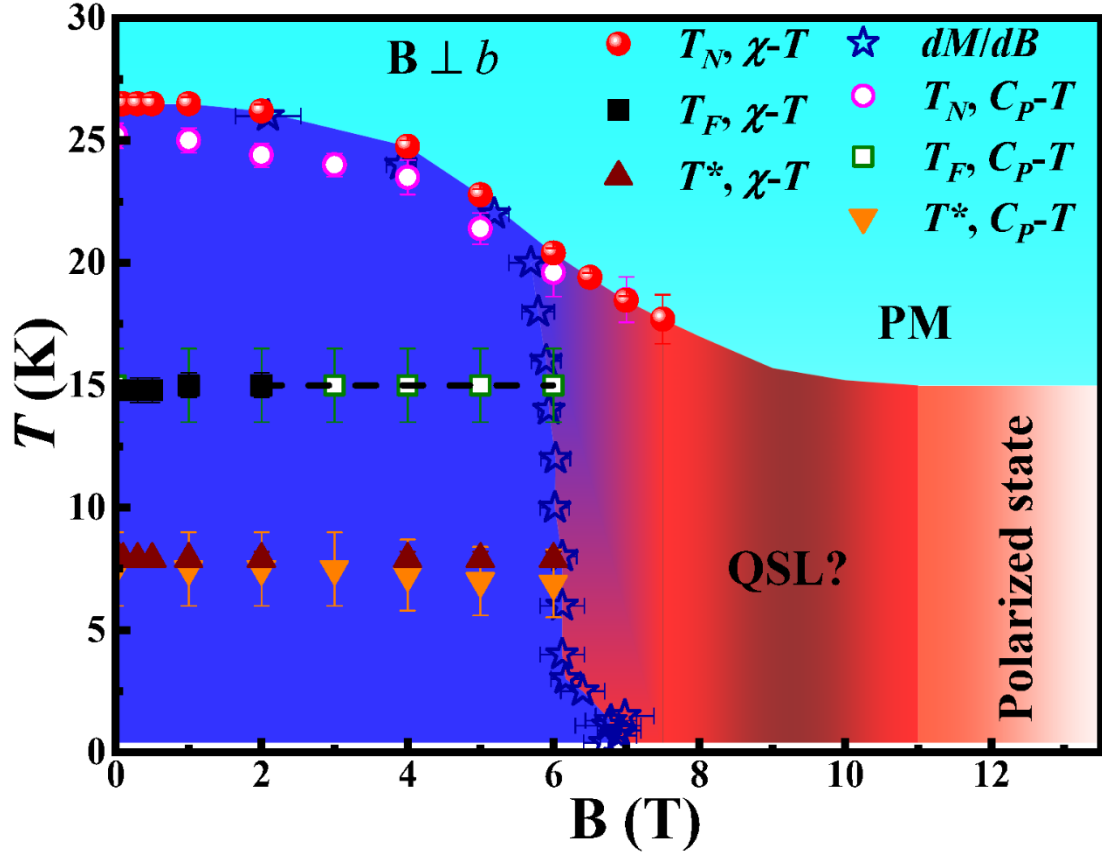


**Fig. 4 Phase diagram of  $\text{Na}_2\text{Co}_2\text{TeO}_6$ .** Temperature-magnetic field phase diagram for NCTO. The stars symbol the first-ordered phase boundary. The color background is used only as a simple guide.

**Spin-wave excitations.** Figure 5a presents the inelastic neutron scattering (INS) measurement with incident energy  $E_i = 11.4$  meV for NCTO at 3 K and two bands (from 0.4 meV to 2.9 meV and from 5.9 meV to 7.1 meV) are observed. The magnetic mode shows an apparent minimum near  $Q = 0.72 \text{ \AA}^{-1}$ , which is close to the magnitude of the M point of the honeycomb reciprocal lattice as expected for a 2D magnetic system. Moreover, the concave shapes are observed at the scattering edges, similar to the magnon excitations observed in other honeycomb lattice magnets with zigzag AFM order of  $\alpha\text{-Na}_2\text{IrO}_3$ <sup>51</sup> and  $\alpha\text{-RuCl}_3$ <sup>12</sup>. As shown in Fig. 5c and d, the INS spectra show a gap of 0.4 meV at the M point. This gap is comparable in energy scale with the ESR gap, which corresponds to the excitation energy at the  $\Gamma$  point.

The diffraction refinement suggested that the magnetic moments were along the crystallographic  $b$  axis with a possible small canting toward the  $c$  axis<sup>40,41</sup>. Since the inter-layer interaction is relatively weak, NCTO could be treated as a single-layer 2D compound at a first approximation. The super-super-exchange Co-O-Te-O-Co pathway

produces a significant third-neighbor exchange interaction  $J_3$ <sup>41</sup>. Meanwhile, the nearest-neighbor Co ions can interact with each other through two 90° Co-O-Co super-exchange paths or direct AFM exchange interactions<sup>35,41</sup>. The cancellation between the different hopping contributions from  $d-d$  and  $d-p-d$  orbits can weaken the ferromagnetic nearest-neighbor  $J$ <sup>52,53</sup>. Together,  $J$  and  $J_3$  can stabilize a zigzag magnetic order. The second neighbor  $J_2$  is likely to be relatively weak in that it tends to destabilize the zigzag order. However, as  $J_{1,2,3}$  is isotropic in the spin space, they cannot select the direction of the magnetic moments; this is achieved by the spin anisotropic interactions such as the  $K$  and  $\Gamma$  terms mentioned in the Introduction.

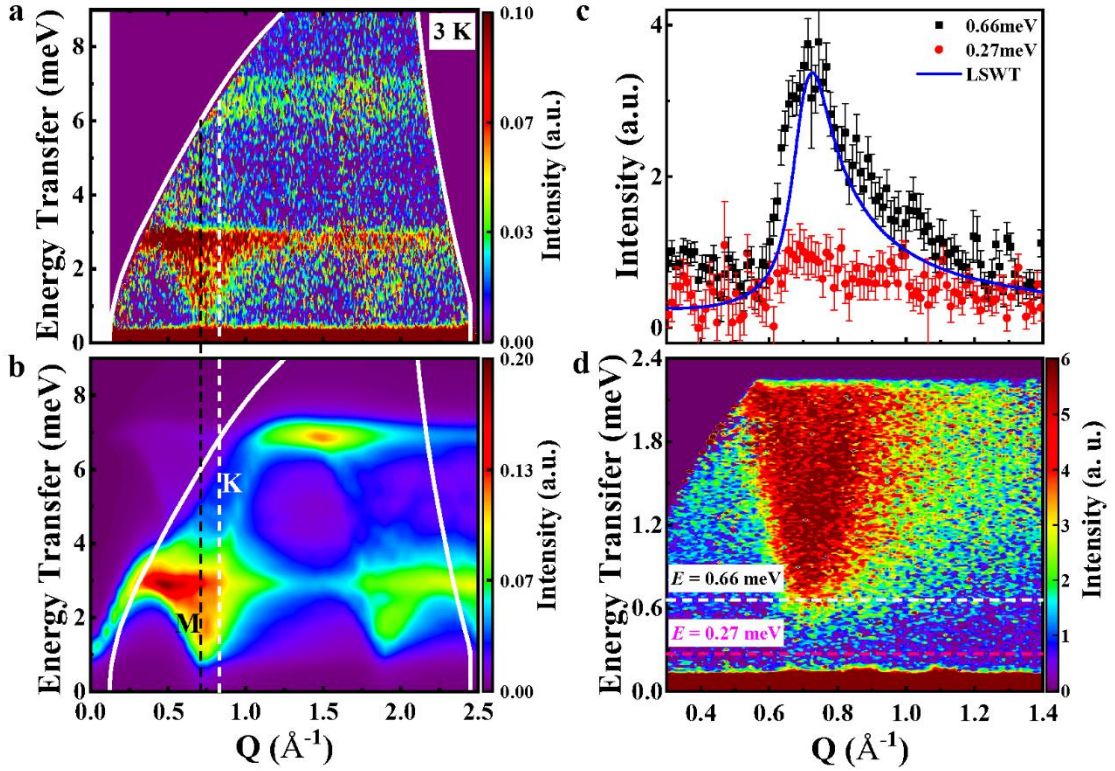


**Fig. 5 Powder INS of  $\text{Na}_2\text{Co}_2\text{TeO}_6$ .** **a** Powder INS using 11.4 meV incident neutron for NCTO at 3 K on spectrometer HRC. The high-temperature data (95 K) was subtracted as background and the thermal effect was simulated by the Bose factor; **b** The calculated powder-averaged scattering including the magnetic form factor with  $K = \Gamma = 0.125$  meV,  $J = -2.325$  meV, and  $J_3 = 2.5$  meV. The black and white dashed lines label M and K points at the first Brillouin zone with  $Q = 0.72$  and  $0.83 \text{ \AA}^{-1}$ , respectively; **c** Constant- $E$  cuts over the energy ranges centered at the locations labeled dashed lines in the Fig. 5d. The solid blue line is constant- $E$  cuts over the energy ranges centered at the 0.66 meV from our LSWT. The absence of structured scattering below 0.4 meV confirms the gap in the magnetic excitation spectrum. **d** Powder inelastic neutron scattering using  $5 \text{ \AA}$  ( $\sim 3.27$  meV) incident neutrons for NCTO at  $T = 3$  K on spectrometer NEAT II, HZB, Deutschland.

The linear spin-wave theory (LSWT) is performed to analyze the INS spectra with

the following exchange Hamiltonians<sup>17-20,22,23</sup>:

$$H = \sum_{\langle i,j \rangle} [J\mathbf{S}_i \cdot \mathbf{S}_j + K S_i^\gamma S_j^\gamma + \Gamma(S_i^\alpha S_j^\beta + S_i^\beta S_j^\alpha)] + J_3 \sum_{\langle\langle i,j \rangle\rangle} \mathbf{S}_i \cdot \mathbf{S}_j \quad (1)$$

where,  $\langle i,j \rangle$  denotes NN sites,  $\mathbf{S}_i$  and  $\mathbf{S}_j$  are effective spin-1/2 operators at site  $i$  and  $j$ , respectively,  $\alpha$  and  $\beta$  are perpendicular to the Kitaev spin axis  $\gamma$ . When the  $J_2$  and  $I$  (Ising exchange interaction) are close to zero (Supplementary 4.1 Symmetries and model), the zigzag AFM order will be more stable. Finally, the powder-averaged scattering numerical results are presented in Fig. 5b. With  $K = \Gamma = 0.125$  meV,  $J = -2.175$  meV, and  $J_3 = 2.5$  meV, the calculated dispersion can reproduce qualitatively the experimental data. While the INS cannot access the excitation energy gap at the  $\Gamma$  point, the LSWT calculation suggests an energy gap on the same order of magnitude as the M point gap, in qualitative agreement with the ESR results.

## DISCUSSION

The characteristic behaviors for the field-induced spin disordered state in NCTO, such as the disappearance of the peaks observed on specific heat and  $\chi(T)$ , the field dependence of magnetic entropy with a maximum near 9 T below 17 K, and the existence of low energy excitations at low temperatures indicated by the  $dM/dB$  curves, are all similar to those observed for the field-induced disordered state above about 7 T in  $\alpha$ -RuCl<sub>3</sub><sup>27,29,30,54-56</sup>. These behaviors have been believed to be evidence that  $\alpha$ -RuCl<sub>3</sub> enters a Kitaev QSL state under fields<sup>27,29,30</sup>. The ESR measurements of  $\alpha$ -RuCl<sub>3</sub> also show extra modes in the field-induced disordered state with a linearly increasing energy gap with increasing magnetic fields<sup>26,33</sup>, similar to that of the D mode observed for NCTO. For  $\alpha$ -RuCl<sub>3</sub>, it has been suggested that when the magnetic field and gap become large enough, it can overcome the energy scale related to the residual Heisenberg interactions so that a QSL emerges<sup>23,26,28,32,33</sup>. While the exact nature of this field-induced disordered state in NCTO needs further studies to determine, the similarities between the disordered states of  $\alpha$ -RuCl<sub>3</sub> and NCTO suggest the possibility of the latter being a QSL state.

We note several recent reports on the magnetic excitations of NCTO with different interpretations<sup>57, 58, 59</sup>. Ref. [57] performs the INS of NCTO on the same facility as this

work but at the higher incident neutron beam energy of 16.54 meV. The resulted INS spectra are qualitatively similar to this work. Moreover, we obtained additional low energy spectra of NCTO with the incident energy of 3.27 meV and achieved better instrument resolution by using another neutron spectrometer NEAT II, HZB, Deutschland. The result (Fig. 5d) shows an energy gap of about 0.4 meV at M-point. It is noticed that Ref. [57] applies different model on the INS spectra. Ref. [57] suggests a large  $J$  (-1.5 meV) and a large AFM  $K$  (3.3 meV), whereas our simulation leads to a large  $J$  (-2.325 meV) and a small AFM  $K$  (0.125 meV). Surprisingly, both could qualitatively reproduce the INS spectra despite different choices for the relative magnitude of the  $K$  term.

Meanwhile, Ref. [58] suggested a small  $J$  (-0.1 meV) and a large FM  $K$  (-9 meV); Ref. [59] compared two sets of exchange interactions, which are  $J$  (-0.2 meV),  $K$  (-7 meV) and  $J$  (-3.2 meV),  $K$  (2.7 meV), respectively. In Ref. [59], it was pointed out that the calculated spectra with the two models, one with FM  $K$  and the other with AFM  $K$ , are almost indistinguishable. Therefore, at this stage, it is difficult to judge which set of exchange interactions is more accurate.

The main reason for the tension among these different fitting parameters, such as a large  $K$  term versus a small  $K$  term, or FM versus AFM  $K$  term, could be due to the fact that all these INS measurements were performed on polycrystalline samples. The powder average effect on the weak signals makes it difficult to determine the Hamiltonian parameters for the complex systems with competing interactions and frustration. Single-crystal neutron scattering measurement in the future is critical to clarify the magnetic structure and dynamics of NCTO while it could be challenging due to the small size of single crystals grown by flux method<sup>44</sup>.

In summary, the most significant finding from our studies on NCTO presented here is a QSL-like disordered state induced under fields with  $7.5 \text{ T} < \mathbf{B} < 10.5 \text{ T}$ . Therefore, NCTO is a novel example of an effective spin-1/2 honeycomb magnet that hosts a field-induced spin disordered state. Its origin, in addition to the related spin structure and spin dynamics, calls for future experimental work on single crystals and

theoretical studies.

## METHODS

**Sample preparation and characterization.** NCTO polycrystalline was prepared by a solid-state reaction method. At first,  $\text{Na}_2\text{CO}_3$  (Alfa, 99.997%),  $\text{Co}_3\text{O}_4$  (Alfa, 99.7%), and  $\text{TeO}_2$  (Alfa, 99.99%) were mixed in a stoichiometric molar ratio with 5% excess  $\text{Na}_2\text{CO}_3$ , and fully ground; then, the mixture was loaded in an alumina crucible and sintered at 850 °C in air for 40 h. The high-quality single crystal was grown by flux method. The polycrystalline sample of NCTO was mixed with the flux of  $\text{Na}_2\text{O}$  and  $\text{TeO}_2$  in molar ratio of 1:0.5:2 and gradually heated to 900 °C at 3 °C/min in air after grinding. The sample was retained at 900 °C for 30 h, and was cooled to a temperature of 500 °C at the rate of 3 °C/h. The furnace was then shut down to cool to room temperature. To confirm the structure and purity of the sample, powder X-ray diffraction (XRD) measurement was performed with a HUBER imaging-plate Guinier camera 670, using  $\text{Cu } K_{\alpha 1}$  radiation ( $\lambda = 1.54051 \text{ \AA}$ ). The XRD patterns were refined with the Rietveld method using the conventional refinement program FullProf (Supplementary Fig. 1). The magnetic properties were checked through measurements as a function of temperature ( $T$ ) and magnetic field ( $B$ ) using a vibrating sample magnetometer (VSM) in the physical properties measurement system (PPMS, Quantum Design). Besides, Magnetization measurements were also carried out using a high-sensitive Hall sensor magnetometer<sup>60-62</sup> for the temperature range from 0.4 K to 30 K. The heat capacity measurements were carried out using the relaxation time method in the PPMS.

**High-field ESR.** The high-field ESR measurements were performed by the high-field high-frequency electron magnetic resonance spectrometer with 25 T water-cooled resistive magnet (field sweep range: 0-25 T, frequency Range: 50-690 GHz, and temperature Range: 2 K-300 K).

**Inelastic neutron scattering.** The inelastic neutron scattering of powder NCTO was performed using the High-Resolution Chopper Spectrometer (HRC) at the J-PARC<sup>63</sup>. The HRC delivers high-resolution and relatively high-energy neutrons for a wide range of studies on materials dynamics. Spectra were collected at various temperatures by operating in high-flux mode (Energy resolution of  $\geq 2\% E_i$ ) with  $E_i = 11.4 \text{ meV}$ . The INS of powder NCTO was also carried out on the recently upgraded cold-neutron direct-geometry time-of-flight spectrometer NEAT II, HZB, Deutschland<sup>64,65</sup>. Each sample was packed in aluminum cans filled with He exchange gas. Each scan was counted around 6 hours with the incident neutron energy  $E_i = 3 \text{ \AA}$  ( $\sim 9 \text{ meV}$ ) and  $5 \text{ \AA}$  ( $\sim$

3.27 meV).

#### **DATA AVAILABILITY**

The data that support the findings of this study are available from the corresponding authors upon request.

## REFERENCES

- 1 Witczak-Krempa, W., Chen, G., Kim, Y. B. & Balents, L. Correlated Quantum Phenomena in the Strong Spin-Orbit Regime. *Annual Review of Condensed Matter Physics* **5**, 57-82, (2014).
- 2 Kitaev, A. Anyons in an exactly solved model and beyond. *Annals of Physics* **321**, 2-111, (2006).
- 3 Jackeli, G. & Khaliullin, G. Mott insulators in the strong spin-orbit coupling limit: from Heisenberg to a quantum compass and Kitaev models. *Phys Rev Lett* **102**, 017205, (2009).
- 4 Hermanns, M., Kimchi, I. & Knolle, J. Physics of the Kitaev Model: Fractionalization, Dynamic Correlations, and Material Connections. *Annual Review of Condensed Matter Physics* **9**, 17-33, (2018).
- 5 Takagi, H., Takayama, T., Jackeli, G., Khaliullin, G. & Nagler, S. E. Concept and realization of Kitaev quantum spin liquids. *Nature Reviews Physics* **1**, 264-280, (2019).
- 6 Kimchi, I., Sheckelton, J. P., McQueen, T. M. & Lee, P. A. Scaling and data collapse from local moments in frustrated disordered quantum spin systems. *Nat Commun* **9**, 4367, (2018).
- 7 Kitagawa, K. *et al.* A spin-orbital-entangled quantum liquid on a honeycomb lattice. *Nature* **554**, 341-345, (2018).
- 8 Hwan Chun, S. *et al.* Direct evidence for dominant bond-directional interactions in a honeycomb lattice iridate  $\text{Na}_2\text{IrO}_3$ . *Nature Physics* **11**, 462-466, (2015).
- 9 Kim, J. *et al.* Dynamic Spin Correlations in the Honeycomb Lattice  $\text{Na}_2\text{IrO}_3$  Measured by Resonant Inelastic x-Ray Scattering. *Physical Review X* **10**, 021034, (2020).
- 10 Choi, S. *et al.* Spin dynamics and field-induced magnetic phase transition in the honeycomb Kitaev magnet  $\alpha\text{-Li}_2\text{IrO}_3$ . *Physical Review B* **99**, (2019).
- 11 Singh, Y. *et al.* Relevance of the Heisenberg-Kitaev model for the honeycomb lattice iridates  $\text{A}_2\text{IrO}_3$ . *Phys Rev Lett* **108**, 127203, (2012).
- 12 Banerjee, A. *et al.* Proximate Kitaev quantum spin liquid behaviour in a honeycomb magnet. *Nat Mater* **15**, 733-740, (2016).
- 13 Nasu, J., Knolle, J., Kovrizhin, D. L., Motome, Y. & Moessner, R. Fermionic response from fractionalization in an insulating two-dimensional magnet. *Nature Physics* **12**, 912-915, (2016).
- 14 Banerjee, A. *et al.* Neutron scattering in the proximate quantum spin liquid  $\alpha\text{-RuCl}_3$ . *Science* **356**, 1055, (2017).
- 15 Do, S.-H. *et al.* Majorana fermions in the Kitaev quantum spin system  $\alpha\text{-RuCl}_3$ . *Nature Physics* **13**, 1079-1084, (2017).
- 16 Rau, J. G., Lee, E. K. & Kee, H. Y. Generic spin model for the honeycomb iridates beyond the Kitaev limit. *Phys Rev Lett* **112**, 077204, (2014).
- 17 Winter, S. M. *et al.* Breakdown of magnons in a strongly spin-orbital coupled magnet. *Nat Commun* **8**, 1152, (2017).
- 18 Wang, J., Normand, B. & Liu, Z. X. One Proximate Kitaev Spin Liquid in the K-J-Gamma Model on the Honeycomb Lattice. *Phys Rev Lett* **123**, 197201, (2019).
- 19 Laurell, P. & Okamoto, S. Dynamical and thermal magnetic properties of the Kitaev spin liquid candidate  $\alpha\text{-RuCl}_3$ . *npj Quantum Materials* **5**, 2, (2020).
- 20 Maksimov, P. A. & Chernyshev, A. L. Rethinking  $\alpha\text{-RuCl}_3$ . *Physical Review Research* **2**, 033011, (2020).
- 21 Ran, K. *et al.* Spin-Wave Excitations Evidencing the Kitaev Interaction in Single Crystalline  $\alpha\text{-RuCl}_3$ . *Phys Rev Lett* **118**, 107203, (2017).
- 22 Hou, Y. S., Xiang, H. J. & Gong, X. G. Unveiling magnetic interactions of ruthenium trichloride

- via constraining direction of orbital moments: Potential routes to realize a quantum spin liquid. *Physical Review B* **96**, 054410, (2017).
- 23 Winter, S. M., Riedl, K., Kaib, D., Coldea, R. & Valenti, R. Probing  $\alpha$ -RuCl<sub>3</sub> Beyond Magnetic Order: Effects of Temperature and Magnetic Field. *Phys Rev Lett* **120**, 077203, (2018).
- 24 Wang, W., Dong, Z.-Y., Yu, S.-L. & Li, J.-X. Theoretical investigation of magnetic dynamics in  $\alpha$ -RuCl<sub>3</sub>. *Physical Review B* **96**, (2017).
- 25 Baek, S. H. *et al.* Evidence for a Field-Induced Quantum Spin Liquid in  $\alpha$ -RuCl<sub>3</sub>. *Phys Rev Lett* **119**, 037201, (2017).
- 26 Ponomaryov, A. N. *et al.* Unconventional spin dynamics in the honeycomb-lattice material  $\alpha$ -RuCl<sub>3</sub>: High-field electron spin resonance studies. *Physical Review B* **96**, 241107(R), (2017).
- 27 Sears, J. A., Zhao, Y., Xu, Z., Lynn, J. W. & Kim, Y.-J. Phase diagram of  $\alpha$ -RuCl<sub>3</sub> in an in-plane magnetic field. *Physical Review B* **95**, 180411, (2017).
- 28 Wang, Z. *et al.* Magnetic Excitations and Continuum of a Possibly Field-Induced Quantum Spin Liquid in  $\alpha$ -RuCl<sub>3</sub>. *Phys Rev Lett* **119**, 227202, (2017).
- 29 Wolter, A. U. B. *et al.* Field-induced quantum criticality in the Kitaev system  $\alpha$ -RuCl<sub>3</sub>. *Physical Review B* **96**, 041405(R), (2017).
- 30 Zheng, J. *et al.* Gapless Spin Excitations in the Field-Induced Quantum Spin Liquid Phase of  $\alpha$ -RuCl<sub>3</sub>. *Phys Rev Lett* **119**, 227208, (2017).
- 31 Banerjee, A. *et al.* Excitations in the field-induced quantum spin liquid state of  $\alpha$ -RuCl<sub>3</sub>. *npj Quantum Materials* **3**, 8, (2018).
- 32 Hentrich, R. *et al.* Unusual Phonon Heat Transport in  $\alpha$ -RuCl<sub>3</sub>: Strong Spin-Phonon Scattering and Field-Induced Spin Gap. *Phys Rev Lett* **120**, 117204, (2018).
- 33 Ponomaryov, A. N. *et al.* Nature of Magnetic Excitations in the High-Field Phase of  $\alpha$ -RuCl<sub>3</sub>. *Physical Review Letters* **125**, 037202, (2020).
- 34 Balz, C. *et al.* Finite field regime for a quantum spin liquid in  $\alpha$ -RuCl<sub>3</sub>. *Physical Review B* **100**, (2019).
- 35 Liu, H. & Khaliullin, G. Pseudospin exchange interactions in  $d^7$  cobalt compounds: Possible realization of the Kitaev model. *Physical Review B* **97**, 014407, (2018).
- 36 Sano, R., Kato, Y. & Motome, Y. Kitaev-Heisenberg Hamiltonian for high-spin  $d^7$  Mott insulators. *Physical Review B* **97**, 014408, (2018).
- 37 Liu, H., Chaloupka, J. & Khaliullin, G. Kitaev Spin Liquid in 3d Transition Metal Compounds. *Phys Rev Lett* **125**, 047201, (2020).
- 38 Zhong, R., Gao, T., Ong, N. P. & Cava, R. J. Weak-field induced nonmagnetic state in a Co-based honeycomb. *Science Advances* **6**, eaay6953, (2020).
- 39 Viciu, L. *et al.* Structure and basic magnetic properties of the honeycomb lattice compounds Na<sub>2</sub>Co<sub>2</sub>TeO<sub>6</sub> and Na<sub>3</sub>Co<sub>2</sub>SbO<sub>6</sub>. *Journal of Solid State Chemistry* **180**, 1060-1067, (2007).
- 40 Lefrançois, E. *et al.* Magnetic properties of the honeycomb oxide Na<sub>2</sub>Co<sub>2</sub>TeO<sub>6</sub>. *Physical Review B* **94**, 214416, (2016).
- 41 Bera, A. K., Yusuf, S. M., Kumar, A. & Ritter, C. Zigzag antiferromagnetic ground state with anisotropic correlation lengths in the quasi-two-dimensional honeycomb lattice compound Na<sub>2</sub>Co<sub>2</sub>TeO<sub>6</sub>. *Physical Review B* **95**, 094424, (2017).
- 42 Bera, A. K. & Yusuf, S. M. Magnetic ground state of the layered honeycomb compound Na<sub>2</sub>Co<sub>2</sub>TeO<sub>6</sub>. *AIP Conference Proceedings* **1942**, 130020, (2018).
- 43 Xiao, G. *et al.* Crystal Growth and the Magnetic Properties of Na<sub>2</sub>Co<sub>2</sub>TeO<sub>6</sub> with Quasi-Two-

- Dimensional Honeycomb Lattice. *Crystal Growth & Design* **19**, 2658-2662, (2019).
- 44 Yao, W. & Li, Y. Ferrimagnetism and anisotropic phase tunability by magnetic fields in  $\text{Na}_2\text{Co}_2\text{TeO}_6$ . *Physical Review B* **101**, 085120, (2020).
- 45 Bordelon, M. M. *et al.* Field-tunable quantum disordered ground state in the triangular-lattice antiferromagnet  $\text{NaYbO}_2$ . *Nature Physics*, (2019).
- 46 Shen, Y. *et al.* Evidence for a spinon Fermi surface in a triangular-lattice quantum-spin-liquid candidate. *Nature* **540**, 559-562, (2016).
- 47 Ramirez, A. P., Hayashi, A., Cava, R. J., Siddharthan, R. & Shastry, B. S. Zero-point entropy in 'spin ice'. *Nature* **399**, 333-335, (1999).
- 48 Broholm, C. *et al.* Quantum spin liquids. *Science* **367**, (2020).
- 49 Li, N. *et al.* Possible itinerant excitations and quantum spin state transitions in the effective spin-1/2 triangular-lattice antiferromagnet  $\text{Na}_2\text{BaCo}(\text{PO}_4)_2$ . *Nat Commun* **11**, 4216, (2020).
- 50 Zvyagin, S. A. *et al.* Direct determination of exchange parameters in  $\text{Cs}_2\text{CuBr}_4$  and  $\text{Cs}_2\text{CuCl}_4$ : high-field electron-spin-resonance studies. *Phys Rev Lett* **112**, 077206, (2014).
- 51 Choi, S. K. *et al.* Spin waves and revised crystal structure of honeycomb iridate  $\text{Na}_2\text{IrO}_3$ . *Phys Rev Lett* **108**, 127204, (2012).
- 52 Winter, S. M., Li, Y., Jeschke, H. O. & Valentí, R. Challenges in design of Kitaev materials: Magnetic interactions from competing energy scales. *Physical Review B* **93**, 214431, (2016).
- 53 Hou, Y. S., Yang, J. H., Xiang, H. J. & Gong, X. G. First-principles study of the magnetic interactions in honeycomb  $\text{Na}_2\text{IrO}_3$ . *Physical Review B* **98**, 094401, (2018).
- 54 Johnson, R. D. *et al.* Monoclinic crystal structure of  $\alpha$ - $\text{RuCl}_3$  and the zigzag antiferromagnetic ground state. *Physical Review B* **92**, 235119, (2015).
- 55 Kubota, Y., Tanaka, H., Ono, T., Narumi, Y. & Kindo, K. Successive magnetic phase transitions in  $\alpha$ - $\text{RuCl}_3$ : XY-like frustrated magnet on the honeycomb lattice. *Physical Review B* **91**, 094422, (2015).
- 56 Yu, Y. J. *et al.* Ultralow-Temperature Thermal Conductivity of the Kitaev Honeycomb Magnet  $\alpha$ - $\text{RuCl}_3$  across the Field-Induced Phase Transition. *Phys Rev Lett* **120**, 067202, (2018).
- 57 Chaebin Kim *et al.* Antiferromagnetic Kitaev interaction in  $J_{\text{eff}} = 1/2$  cobalt honeycomb materials  $\text{Na}_3\text{Co}_2\text{SbO}_6$  and  $\text{Na}_2\text{Co}_2\text{TeO}_6$ . *arXiv:2012.06167*, (2020).
- 58 Songvilay, M. *et al.* Kitaev interactions in the Co honeycomb antiferromagnets  $\text{Na}_3\text{Co}_2\text{SbO}_6$  and  $\text{Na}_2\text{Co}_2\text{TeO}_6$ . *Physical Review B* **102**, 224429, (2020).
- 59 Anjana M. Samarakoon, Qiang Chen, Haidong Zhou & Garlea, V. O. Static and dynamic magnetic properties of honeycomb lattice antiferromagnets  $\text{Na}_2\text{M}_2\text{TeO}_6$ ,  $\text{M} = \text{Co}$  and  $\text{Ni}$  *arXiv:2105.06549v1*, (2021).
- 60 Candini, A. *et al.* Hall nano-probes fabricated by focused ion beam. *Nanotechnology* **17**, 2105-2109, (2006).
- 61 Cavallini, A., Fraboni, B., Capotondi, F., Sorba, L. & Biasiol, G. Deep levels in MBE grown AlGaAs/GaAs heterostructures. *Microelectronic Engineering* **73-74**, 954-959, (2004).
- 62 Candini, A. & Affronte, M. *Magnetometry by means of Hall microprobes in the Quantum Design PPMS*. Vol. 1084-701 (Application Note, 2008).
- 63 Itoh, S. *et al.* High Resolution Chopper Spectrometer (HRC) at J-PARC. *Nuclear Instruments and Methods in Physics Research Section A: Accelerators, Spectrometers, Detectors and Associated Equipment* **631**, 90-97, (2011).
- 64 Günther, G. & Russina, M. Background optimization for the neutron time-of-flight spectrometer

NEAT. *Nuclear Instruments and Methods in Physics Research Section A: Accelerators, Spectrometers, Detectors and Associated Equipment* **828**, 250-261, (2016).

65 Russina, M. *et al.* Upgrade project NEAT'2016 at Helmholtz Zentrum Berlin – What can be done on the medium power neutron source. *Physica B: Condensed Matter* **551**, 506-511, (2018).

## **Acknowledgments**

G.T. L, Y.W., Z.Q., W.T., L.S.L, C.Y.X and J.M. thank the financial support from the National Key Research Development Program of China (Grant No. 2016YFA0300501, 2018YFA0704300, and 2016YFA0401802) and the National Science Foundation of China (No. U2032213, 11774223, U1732154, 12004243, 11974396, U1832214, and No. 11774352). G.T.L thanks the project funded by China Postdoctoral Science Foundation (Grant No. 2019M661474). J.M. thanks a Shanghai talent program. Y.W. thanks the Strategic Priority Research Program of the Chinese Academy of Sciences (Grant No. XDB33020300). Q.H. and H.D.Z. thank the support from NSF-DMR-2003117. Work at the CQM and SNU was supported by the Leading Researchers Program of the National Research Foundation of Korea (Grant No. 2020R1A3B2079375). A portion of this work was supported by the High Magnetic Field Laboratory of Anhui Province. The INS experiment was performed at the MLF of J-PARC under a user program (proposal No. 2019B0350).

## **Author contributions**

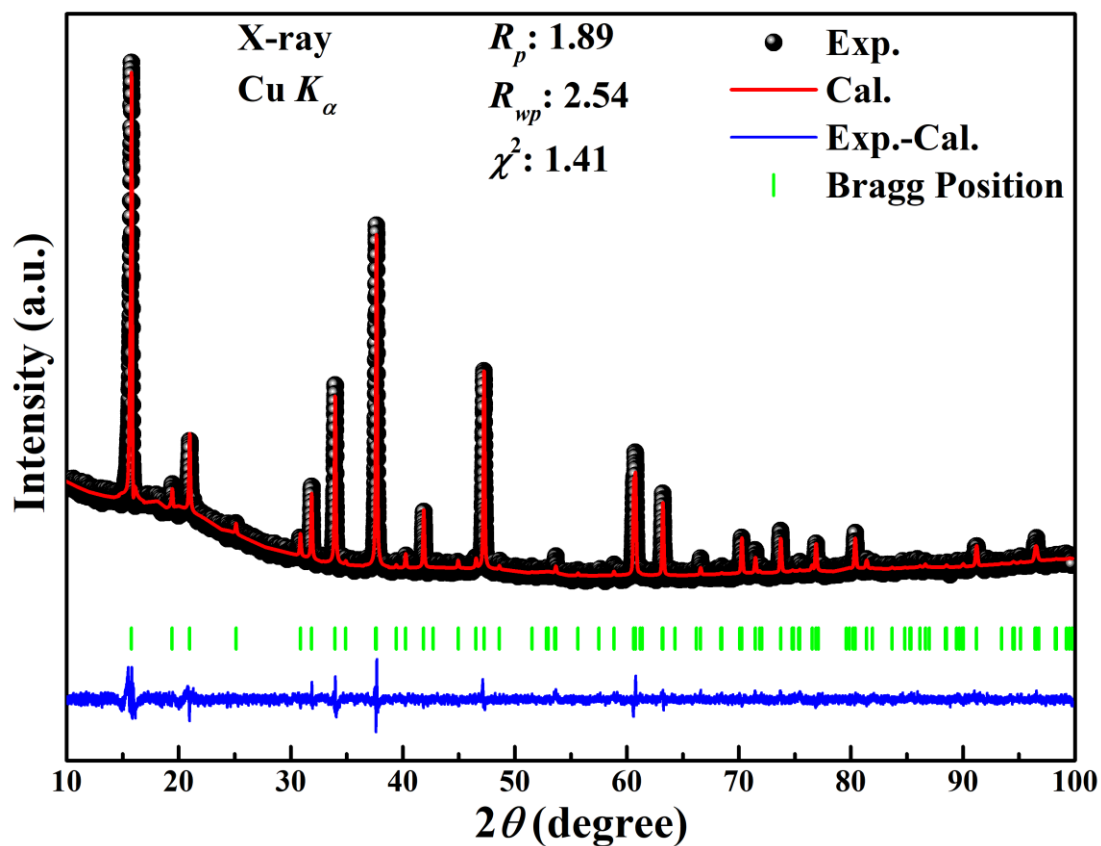
G.T.L., Y.W., H.D.Z., and J.M. conceived the project. Q.H. performed the XRD measurement and analyzed the data with help from G.T.L., Q.Y.R., and G.H.W. G.T.L, J.M.S., Q.H., and G.H.W. performed magnetization and heat capacity measurements and analyzed the data with help from J.C.W., Z.X.L, L.S.W., Z.Q., J.M., and H.D.Z. Q.H., L.W., J.W.M, and H.D.Z. synthesized the samples. J.J, C.K., T.M., S.A., S.I., G.G., M.R., Z.L., and J.M. performed neutron scattering measurements and analyzed the data with help from J.G.P., G.T.L., Q.Y.R., G.H.W., and Y.W. W.T., C.Y.X, L.S.L., and G.T.L. performed high-field ESR measurements. Y.W. and Y.W. performed LSWT calculations with help from X.Q.W. G.T.L., J.M., Y.W., and H.D.Z. wrote the paper with input from all other co-authors. All authors discussed the data and its interpretation.

## **Competing Interests**

The authors declare no competing interests.

## Supplemental Material

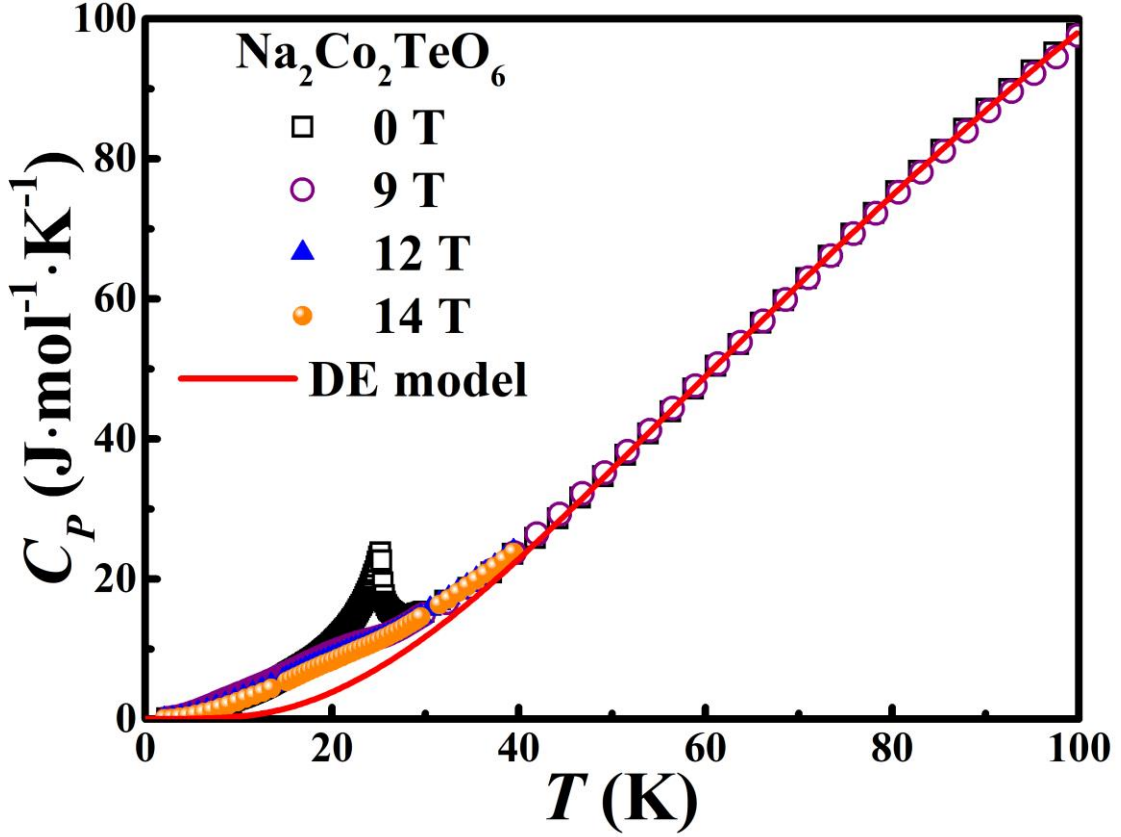
### 1. Crystal structure



**Supplementary Figure 1: Powder X-ray diffraction of  $\text{Na}_2\text{Co}_2\text{TeO}_6$ .** The powder x-ray diffraction pattern was recorded using  $\text{Cu } K_\alpha$  radiation at room temperature. The difference between experimental and calculated patterns is shown by the blue solid lines. The vertical bars indicate the positions of allowed Bragg peaks.

The measured diffraction patterns were analyzed by using the Rietveld refinement technique (by employing the FULLPROF computer program). The Rietveld analysis reveals that the compound crystallizes in the hexagonal symmetry with space group P6322 (No. 182).

## 2. Heat capacity



**Supplementary Figure 2: Heat capacity of  $\text{Na}_2\text{Co}_2\text{TeO}_6$  under different field.** Heat capacity  $C_P$  as a function of  $T$  for NCTO. The red line is the calculated  $C_V(T)$  using Eq. S(1).

Since NCTO is a Mott insulator [1,2], the electronic contribution to the heat capacity is not considered. Hence, for a reasonable description of lattice heat capacity  $C_V(T)$ , a combined Debye-Einstein (DE) model should be employed, where  $C_V(T)$  is defined by the following expression [3]:

$$C_V(T) = 9R \frac{\sum_{i=1}^3 a_i}{n-1} x_D^{-3} \int_0^{x_D} \frac{x^4 e^x}{(e^x - 1)^2} dx + 3R \sum_{i=1}^3 \left[ a_i \frac{x_{E_i}^2 e^{x_{E_i}}}{(e^{x_{E_i}} - 1)^2} \right], \quad \text{S(1)}$$

where  $x_D$  and  $x_E$  are defined via  $x_D = \Theta_D/T$  and  $x_E = \Theta_E/T$ ,  $\Theta_D$  and  $\Theta_E$  are the Debye and Einstein temperatures, respectively. The parameter  $n$  is the number of atoms per formula unit, and  $R$  is the molar gas constant. The constants  $a_i$  are adjust parameters. The first term in Eq. S(1) represents the Debye heat capacity related to the acoustic modes, and the second term is a sum of Einstein phonon contributions related to optic modes. The

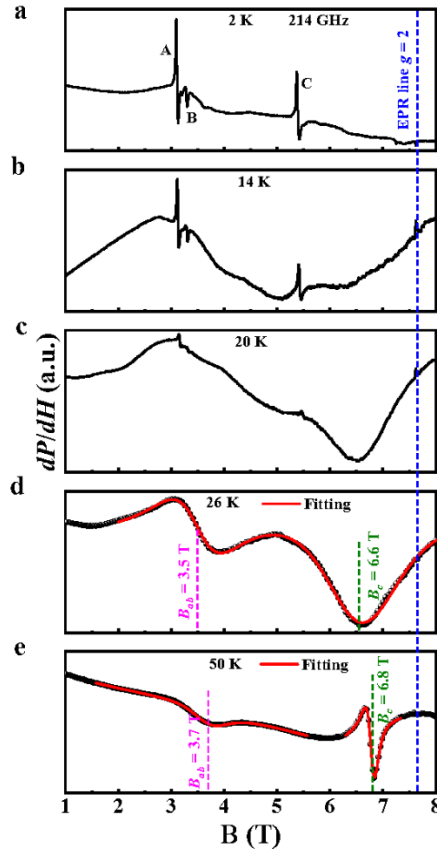
red curve shows the fitted  $C_P(T)$  by Eq. S(1) over the temperature range from about 2 to 100 K in Supplementary Fig. 1 using the  $\Theta_D = 160.2$  K,  $\Theta_{E_1} = 113.9$  K,  $\Theta_{E_2} = 234.6$  K,  $\Theta_{E_3} = 467.8$  K. Hence, we can extract the magnetic contribution  $C_{\text{mag}}(T)$  from the measured  $C_P(T)$ ,  $C_{\text{mag}}(T) = C_P(T) - nC_V(T)$ .

### 3. High-field electron spin resonance

The EPR spectra are well fitted by Dysonian line shape given by:

$$\frac{dP}{dB} \propto \frac{d}{dB} \left[ \frac{2\Delta B + 4a(B - B_r)}{\Delta B^2 + 4(B - B_r)^2} + \frac{2\Delta B + 4a(B + B_r)}{\Delta B^2 + 4(B + B_r)^2} \right]. \quad S(2)$$

This is an asymmetric Lorentzian line, which includes absorption and dispersion, denoting the dispersion-to-absorption (D/A) ratio.  $B_r$  and  $\Delta B$  are the resonance field and full-linewidth at half-maximum, respectively. Compared to the fitted results of 26 K, higher resonance fields at 50 K indicate the presence of short-range magnetic correlations above  $T_N$  (Supplementary Fig. 3).



**Supplementary Figure 3: ESR spectra of  $\text{Na}_2\text{Co}_2\text{TeO}_6$  at different temperatures.** ESR spectra with the frequency  $\nu = 214$  GHz at different temperatures. A weak but observable EPR signal marked with a blue dashed line indicates PM impurities in our sample, not affected by our results. The red lines are the fitted EPR lines using Eq. S(2).

## 4. Linear spin-wave theory for zigzag ground states

### 4.1 Symmetries and model

The space group of NCTO is P6<sub>3</sub>22 (No.182). This material can be naturally viewed as a magnetic bilayer with AB stacking. Co<sup>2+</sup> ions at crystallographic positions (0, 0, 1/4) (Wyckoff position 2*b*) and (2/3, 1/3, 1/4) (Wyckoff position 2*d*) form the first layer (Supplementary Fig. 4a). The system possesses a 3-fold rotational symmetry at these sites with respect to the crystallographic *c* axis and 2-fold rotational symmetry with respect to the three-neighboring links. Co<sup>2+</sup> at (0, 0, 3/4) (Wyckoff position 2*b*) and (1/3, 2/3, 3/4) (Wyckoff position 2*d*) form the second layer. The symmetry properties of the second layer are identical to the first.

To understand the dynamical spin-spin correlations, we compare the INS data to the solution of H-K Hamiltonian using conventional LSWT for zigzag order. We propose a phenomenological, symmetry-constrained pseudo-spin  $J_{\text{eff}} = 1/2$  exchange Hamiltonian for this material. We neglect the interlayer coupling as the previous analysis seems to suggest it to be weak. Consider a pair of nearest neighbors *ij*, where  $i \in A$  and  $j \in B$ . The 2-fold rotational symmetry with respect to the bond *ij* allows the following exchange interactions:

$$H_{ij} = J_I \mathbf{S}_i \cdot \mathbf{S}_j + I S_i^c S_j^c + J_K (\mathbf{S}_i \cdot \hat{n}_{ij})(\mathbf{S}_j \cdot \hat{n}_{ij}) + (J_G + J_D)(\mathbf{S}_i \cdot \hat{\varepsilon}_{ij})S_j^c + (J_G - J_D)(\mathbf{S}_j \cdot \hat{\varepsilon}_{ij})S_i^c \quad \text{S(3)}$$

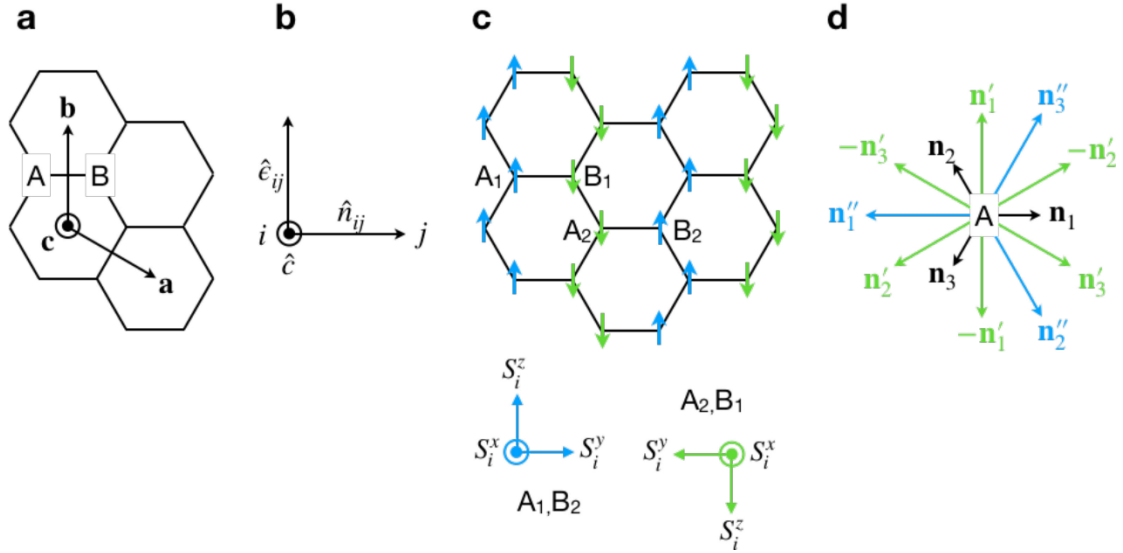
Here  $S_i^c$  is the projection of the spin along the crystallographic *c* axis.  $\hat{n}_{ij}$  is the unit vector pointing from site *i* to *j*,  $\hat{\varepsilon}_{ij} \equiv \hat{c} \times \hat{n}_{ij}$ . Therefore,  $\{\hat{n}_{ij}, \hat{\varepsilon}_{ij}, \hat{c}\}$  form a (link dependent) right-hand frame (Supplementary Fig. 4b). The 2-fold rotational symmetry with respect to  $\hat{n}_{ij}$  forbids the coupling between the spin component parallel with the  $\hat{n}_{ij}$  axis and the components orthogonal to it. This eliminates 4 coupling constants.  $3 \times 3 - 4 = 5$  coupling constants remain.

We recognize *I* as the Ising exchange interaction,  $J_K$  as the pseudo-dipolar interaction,  $J_D$  the DM (Dzyaloshinskii–Moriya) interaction, and finally,  $J_G$  the symmetric off-diagonal interaction. Crucially, the pseudo-dipolar interaction is not the Kitaev interaction proposed by J. Chaloupka et al. [4] in that the said Kitaev interaction

uses a spin coordinate system different from here. However, it is possible to express the said Kitaev interaction in terms of these coupling constants. We also would like to include the second and third neighbor exchange interactions. Liu and Khaliullin [1] argue that the further neighbor exchange interactions tend to be more isotropic as the spin anisotropy resulted from different superexchange paths average out.

We thus take these further neighbor exchange interactions to be of Heisenberg type. Hence, we write the Hamiltonian as  $H = H^{(I)} + H^{(II)}$ , where  $H^{(I)}$  and  $H^{(II)}$  respectively describe the first and second layer:

$$H^{(k)} = \sum_{\langle ij \rangle \in k} H_{ij} + J_2 \sum_{\langle\langle ij \rangle\rangle \in k} \mathbf{S}_i \cdot \mathbf{S}_j + J_3 \sum_{\langle\langle\langle ij \rangle\rangle\rangle \in k} \mathbf{S}_i \cdot \mathbf{S}_j. \quad (k = \text{I, II}). \quad \text{S(4)}$$



**Supplementary Figure 4: Structure of  $\text{Na}_2\text{Co}_2\text{TeO}_6$ .** **a** A single layer of the honeycomb lattice.  $a, b, c$  is the crystallographic primitive vectors. A and B label the two crystallographic sublattices. **b** The right-hand frame is associated with a link  $ij$ . **c** Zigzag ground state.  $A_{1,2}$  and  $B_{1,2}$  label the magnetic sublattices. The local spin frames are also shown. **d** The nearest, second, and third neighbors of an A sublattice site and the associated vectors.

The first, second, and third summations are, respectively, over nearest, second, and third neighbors in the same layer (Supplementary Fig. 4d). However, since it has been shown experimentally that the inter-layer spin correlations are short-ranged, we shall treat the layers as independent and perform all the calculations in the effective single-layer model.

## 4.2 Constraining model parameters

The experiment has shown that NCTO shows zigzag order in its ground state. Refinement suggests that the magnetic moments are along the crystallographic  $b$  axis with a small  $c$  component. As a first approximation, we may take the moments to be in the basal plane. This implies that  $J_F$  and  $J_D$  must be approximately zero.

One of the symmetry-equivalent zigzag orders is shown in Supplementary Fig. 4c. There are four magnetic sublattices, labeled  $A_{1,2}$  and  $B_{1,2}$ . We compute the Weiss molecular field on each spin. We find the molecular fields due to the  $J_F$  and  $J_D$  terms are all along the crystallographic  $c$  axis:

$$h_i^c = \begin{cases} 2(J_F - J_D)S & (i \in A_1) \\ -2(J_F - J_D)S & (i \in A_2) \\ -2(J_F + J_D)S & (i \in B_1) \\ 2(J_F + J_D)S & (i \in B_2) \end{cases} \quad \text{S(5)}$$

For the magnetic moment to be in the basal plane, the molecular fields along the crystallographic  $c$  axis must vanish. This implies  $J_F = J_D = 0$ .

The independent parameters are thus  $J_{1,2,3}$ ,  $J_K$ , and  $I$ . The previous analysis has shown that the  $J_1$ - $J_2$ - $J_3$  model may stabilize the zigzag type magnetic order. However,  $J_{1,2,3}$  alone, being isotropic in spin space, cannot force the magnetic moments to be in any particular direction — this is achieved by  $J_K$  and  $I$ . We now determine the sign of  $J_K$  and  $I$ . To this end, we consider the following trial state: the spins form a collinear zigzag order similar to Supplementary Fig. 4c. The magnetic moment takes a direction  $\hat{m}$  that is not necessarily along the crystallographic  $b$  axis. The energy per unit cell is given by:

$$\frac{E(\hat{m})}{N_{cell}} = -\frac{J_K}{2}(m^{a^*})^2 + \frac{3J_K}{2}(m^b)^2 + I(m^c)^2. \quad \text{S(6)}$$

Here,  $m^{a^*}$ ,  $m^b$ , and  $m^c$  are the projection of  $\hat{m}$  along the  $a^*$ ,  $b$ , and  $c$  axis. For the moment to be in the  $b$  axis, we must have:

$$J_K < 0, \quad I > -\frac{3|J_K|}{2}. \quad \text{S(7)}$$

### 4.3 Spin wave calculations

We now compute the spin-wave spectrum. For the sake of simplicity, we set  $J_2 = I = 0$ . To this end, we orient the local spin frames such that the local  $S_i^z$  axis coincides with the magnetic moment in the ground state. The specific choices are given in Supplementary Fig. 4c. We then employ the Holstein-Primakoff transformation to the leading order in  $1/S$ :

$$S_r^x = \sqrt{S}x_r; \quad S_r^y = \sqrt{S}y_r; \quad S_r^z = S - \frac{x_r^2 + y_r^2}{2}. \quad \text{S(8)}$$

where  $x_r$  and  $y_r$  obey the commutation relation:  $[x_r, y_r] = i$ . Substituting it into the Hamiltonian  $H^{(1)}$  and expand to the second-order,

$$\begin{aligned} H^{(1)} = & \frac{-J_1S + 3J_3S - 3J_KS/2}{2} \sum_r (x_r^2 + y_r^2) + J_1S \sum_{r \in A} \sum_i x_r x_{r+n_i} + J_3S \sum_{r \in A} \sum_i x_r x_{r+n_i} \\ & - \sum_{r \in A} (J_1 + J_K) y_r y_{r+n_1} + (J_1 + \frac{J_K}{4}) y_r y_{r+n_2} + (J_1 + \frac{J_K}{4}) y_r y_{r+n_3} - J_3S \sum_{r \in A} \sum_i y_r y_{r+n_i}. \end{aligned} \quad \text{S(9)}$$

Here  $\mathbf{n}_{1,2,3}$ ,  $\pm\mathbf{n}'_{1,2,3}$ , and  $\mathbf{n}''_{1,2,3}$  are vectors associated with the nearest, second, and third neighbors. Their definitions are given in Supplementary Fig. 4d.

We note that Hamiltonian's translation symmetry is the same as the lattice (i.e., higher than the translation symmetry of the magnetic ground state). Thus, we may block diagonalize the Hamiltonian by switching to the momentum space:

$$x_r = \frac{1}{\sqrt{N_{cell}}} \sum_{\mathbf{q} \in \text{1BZ}} x_{A/B}(\mathbf{q}) \exp(i\mathbf{q} \cdot \mathbf{r}), \quad y_r = \frac{1}{\sqrt{N_{cell}}} \sum_{\mathbf{q} \in \text{1BZ}} y_{A/B}(\mathbf{q}) \exp(i\mathbf{q} \cdot \mathbf{r}). \quad \text{S(10)}$$

where the summation is over the first BZ (rather than the magnetic BZ). The commutation relation is:  $[x_a(\mathbf{q}), y_a(-\mathbf{q})] = i$ . The Hamiltonian now reads,

$$\begin{aligned} H^{(1)} = & \frac{1}{2} \sum_{\mathbf{q}} x^\dagger(\mathbf{q}) X(\mathbf{q}) x(\mathbf{q}) + y^\dagger(\mathbf{q}) Y(\mathbf{q}) y(\mathbf{q}) \\ = & \frac{1}{2} \sum_{\mathbf{k}} (x_A(-\mathbf{q}), x_B(-\mathbf{q})) \begin{pmatrix} X_{AA}(\mathbf{q}) & X_{AB}(\mathbf{q}) \\ X_{AB}^*(\mathbf{q}) & X_{AA}(\mathbf{q}) \end{pmatrix} \begin{pmatrix} x_A(\mathbf{k}) \\ x_B(\mathbf{k}) \end{pmatrix} \\ & + (y_A(-\mathbf{q}), y_B(-\mathbf{q})) \begin{pmatrix} Y_{AA}(\mathbf{q}) & Y_{AB}(\mathbf{q}) \\ Y_{AB}^*(\mathbf{q}) & Y_{AA}(\mathbf{q}) \end{pmatrix} \begin{pmatrix} y_A(\mathbf{k}) \\ y_B(\mathbf{k}) \end{pmatrix}, \end{aligned} \quad \text{S(11)}$$

where

$$\begin{aligned}
X_{AA}(\mathbf{q})/S &= -J_1 - 3J_K/2 + 3J_3; \\
X_{AB}(\mathbf{q})/S &= J_1 \sum_i e^{i\mathbf{q}\cdot\mathbf{n}_i} + J_3 \sum_i e^{i\mathbf{q}\cdot\mathbf{n}_i^*}; \\
Y_{AA}(\mathbf{q})/S &= -J_1 - 3J_K/2 + 3J_3; \\
Y_{AB}(\mathbf{q})/S &= -(J_1 + J_K)e^{i\mathbf{q}\cdot\mathbf{n}_1} + (J_1 + J_K/4) \sum_{i=2,3} e^{i\mathbf{q}\cdot\mathbf{n}_i} - J_3 \sum_i e^{i\mathbf{q}\cdot\mathbf{n}_i^*}.
\end{aligned}$$

Note  $X(\mathbf{q})$  and  $Y(\mathbf{q})$  must be positive semi-definite for all  $\mathbf{q}$ .

We are now ready to diagonalize the Hamiltonian  $H^{(I)}$ . To this end, we perform the SVD:

$$X(\mathbf{q})^{1/2}Y(\mathbf{q})^{1/2} = U(\mathbf{q})\Omega(\mathbf{q})V^\dagger(\mathbf{q}). \Rightarrow Y(\mathbf{q})^{1/2}X(\mathbf{q})^{1/2} = V(\mathbf{q})\Omega(\mathbf{q})U(\mathbf{q})^\dagger. \quad \text{S(12)}$$

$\Omega(\mathbf{q}) = \text{diag}(\omega_1(\mathbf{q}), \omega_2(\mathbf{q}))$ . The second equation follows from the first by the hermiticity of  $X(\mathbf{q})$  and  $Y(\mathbf{q})$ . Furthermore,

$$X(\mathbf{q})^* = X(-\mathbf{q}), Y(\mathbf{q})^* = Y(-\mathbf{q}). \Rightarrow U(\mathbf{q})^* = U(-\mathbf{q}), V(\mathbf{q})^* = V(-\mathbf{q}), \Omega(\mathbf{q})^* = \Omega(-\mathbf{q}). \quad \text{S(13)}$$

The latter relations may be used as a gauge-fixing condition on  $U(\mathbf{q}), V(\mathbf{q})$ . We define a new set of variables:

$$\begin{aligned}
x_\alpha(\mathbf{q}) &= \sum_\lambda \left[ (Y(\mathbf{q}))^{1/2} V(\mathbf{q}) \right]_{\alpha\lambda} \frac{b_\lambda(\mathbf{q}) + b_\lambda^\dagger(-\mathbf{q})}{\sqrt{2\omega_\lambda(\mathbf{q})}}; \\
y_\alpha(\mathbf{q}) &= \sum_\lambda \left[ (X(\mathbf{q}))^{1/2} U(\mathbf{q}) \right]_{\alpha\lambda} \frac{b_\lambda(\mathbf{q}) - b_\lambda^\dagger(-\mathbf{q})}{i\sqrt{2\omega_\lambda(\mathbf{q})}}.
\end{aligned} \quad \text{S(14)}$$

Here,  $\alpha = A, B$ ,  $\lambda = 1, 2$  labels the two spin wave branches.  $b_\lambda(\mathbf{k})$  annihilates a magnon with label  $\lambda$  and momentum  $\mathbf{k}$ .  $\omega_\lambda(\mathbf{k})$  is the dispersion relation of the spin-wave. It's straightforward to show that the above transformation preserves the commutation relations and constitutes a canonical transformation. Substituting the above into  $H^{(I)}$ ,

$$H^{(I)} = \sum_{\mathbf{k}\lambda} \omega_\lambda(\mathbf{k}) \left( b_\lambda^\dagger(\mathbf{k}) b_\lambda(\mathbf{k}) + 1/2 \right) \quad \text{S(15)}$$

As  $H^{(II)}$  is isomorphic to  $H^{(I)}$ , it is diagonalized in the same vein.

#### 4.4 Dynamic spin structure factor

We now compute the dynamic spin structure factor  $S^{ab}(\mathbf{q}, \omega)$ . We first relate the Fourier transform of the magnetic moment to  $x_{A,B}(\mathbf{q})$  and  $y_{A,B}(\mathbf{q})$ :

$$\mu^{a*}(\mathbf{q}) = \sqrt{S} [y_A(\mathbf{q} + \mathbf{G}_1/2) - e^{i\frac{2\pi}{3}} y_B(\mathbf{q} + \mathbf{G}_1/2)]; \quad \mu^c(\mathbf{q}) = \sqrt{S} [x_A(\mathbf{q}) + x_B(\mathbf{q})]. \quad \text{S(16)}$$

We have omitted the Bohr magneton, etc. Note  $\hat{a}^*, \hat{b}, \hat{c}$  form an orthogonal frame (the

crystallographic  $\hat{a}$ ,  $\hat{b}$ ,  $\hat{c}$  do not form orthogonal frame). The  $b$  direction is the ordering direction of the magnetic moment; scattering in this direction only produces elastic component within the quadratic approximation and shall be omitted.  $\mathbf{G}_1/2$  is the ordering wave vector.

The additional phase factor  $\exp(-i\frac{2\pi}{3})$  requires explanation. The boost vector  $\mathbf{G}_1/2$  accounts for the staggering of the local  $S^y$  axis. However, it introduces an unwanted phase difference  $-(\mathbf{n}_1 \cdot \mathbf{G}_1)/2 = -2\pi/3$  between the A and B sub-lattices. The factor mentioned above cancels this phase difference:

$$\begin{aligned}\mu^{a^*}(\mathbf{q}) &\approx \sum_{r \in A_1} y_r e^{-i\mathbf{q}\mathbf{r}} - \sum_{r \in A_2} y_r e^{-i\mathbf{q}\mathbf{r}} - \sum_{r \in B_1} y_r e^{-i\mathbf{q}\mathbf{r}} - \sum_{r \in B_2} y_r e^{-i\mathbf{q}\mathbf{r}} \\ &= \sum_{r \in A_1} y_r e^{-i(\mathbf{q}+\mathbf{G}_1/2)\mathbf{r}} + \sum_{r \in A_2} y_r e^{-i(\mathbf{q}+\mathbf{G}_1/2)\mathbf{r}} - \sum_{r \in B_1} y_r e^{-i(\mathbf{q}+\mathbf{G}_1/2)(\mathbf{r}-\mathbf{n}_1)} - \sum_{r \in B_2} y_r e^{-i(\mathbf{q}+\mathbf{G}_1/2)(\mathbf{r}-\mathbf{n}_1)} \quad \text{S(17)} \\ &= y_A(\mathbf{q} + \mathbf{G}_1/2) - e^{i\frac{2\pi}{3}} y_B(\mathbf{q} + \mathbf{G}_1/2).\end{aligned}$$

We thus find the dynamic spin structure factors at zero temperature:

$$\begin{aligned}S^{a^*a^*}(\mathbf{q}, \omega) &= S \sum_{\lambda} Z_{\lambda}^{a^*}(\mathbf{q} + \mathbf{G}_1/2) \delta(\omega - \omega_{\lambda}(\mathbf{q} + \mathbf{G}_1/2)). \\ S^{cc}(\mathbf{q}, \omega) &= S \sum_{\lambda} Z_{\lambda}^c(\mathbf{q}) \delta(\omega - \omega_{\lambda}(\mathbf{q})).\end{aligned} \quad \text{S(18)}$$

The cross-correlations vanish due to the momentum mismatch. The spectral weights  $Z_{\lambda}^{a^*}(\mathbf{q})$  and  $Z_{\lambda}^c(\mathbf{q})$  are given by

$$\begin{aligned}Z_{\lambda}^{a^*}(\mathbf{q}) &= \frac{1}{2\omega_{\lambda}(\mathbf{q})} \left[ U(\mathbf{q})^{\dagger} X(\mathbf{q})^{1/2} \begin{pmatrix} 1 & -e^{i\frac{2\pi}{3}} \\ -e^{-i\frac{2\pi}{3}} & 1 \end{pmatrix} X(\mathbf{q})^{1/2} U(\mathbf{q}) \right]_{\lambda\lambda} \quad \text{S(19)} \\ Z_{\lambda}^c(\mathbf{q}) &= \frac{1}{2\omega_{\lambda}(\mathbf{q})} \left[ V(\mathbf{q})^{\dagger} Y(\mathbf{q})^{1/2} \begin{pmatrix} 1 & 1 \\ 1 & 1 \end{pmatrix} Y(\mathbf{q})^{1/2} V(\mathbf{q}) \right]_{\lambda\lambda}.\end{aligned}$$

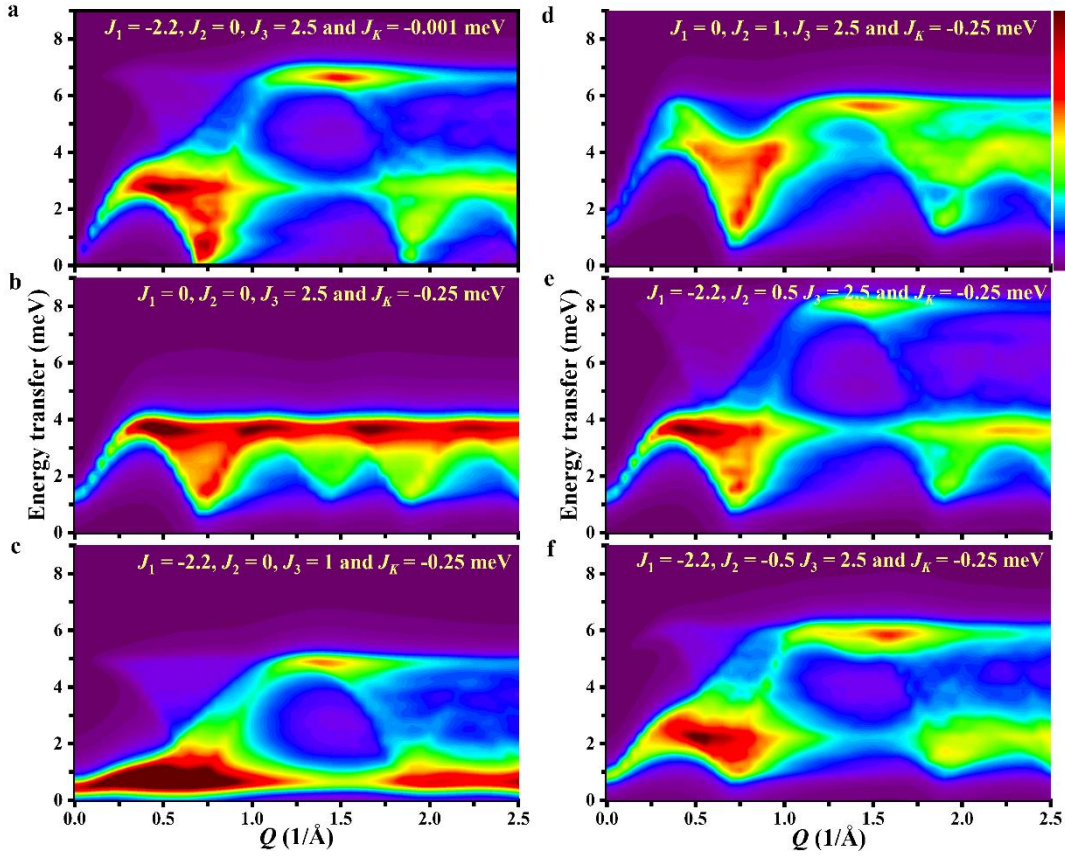
We are now ready to compute the powder average. We first note that the nominal bilayer system is equivalent to a single layer system as we have assumed no correlation between the two layers. Furthermore,  $S^{a\beta}(\mathbf{q}, \omega)$  only depends on the in-plane component. Let  $\mathbf{q} = q(\cos\phi\sin\theta, \sin\phi\sin\theta, \cos\theta)$ . Here, the three components are expressed in those mentioned above  $a^*bc$  orthogonal frame. The cross-section is given by:

$$I(q, \theta, \phi, \omega) = (1 - \sin^2 \theta \cos^2 \phi) S^{a^*a^*}(q \sin \theta \cos \phi, q \sin \theta \sin \phi, \omega) + \sin^2 \theta S^{cc}(q \sin \theta \cos \phi, q \sin \theta \sin \phi, \omega). \quad \text{S(20)}$$

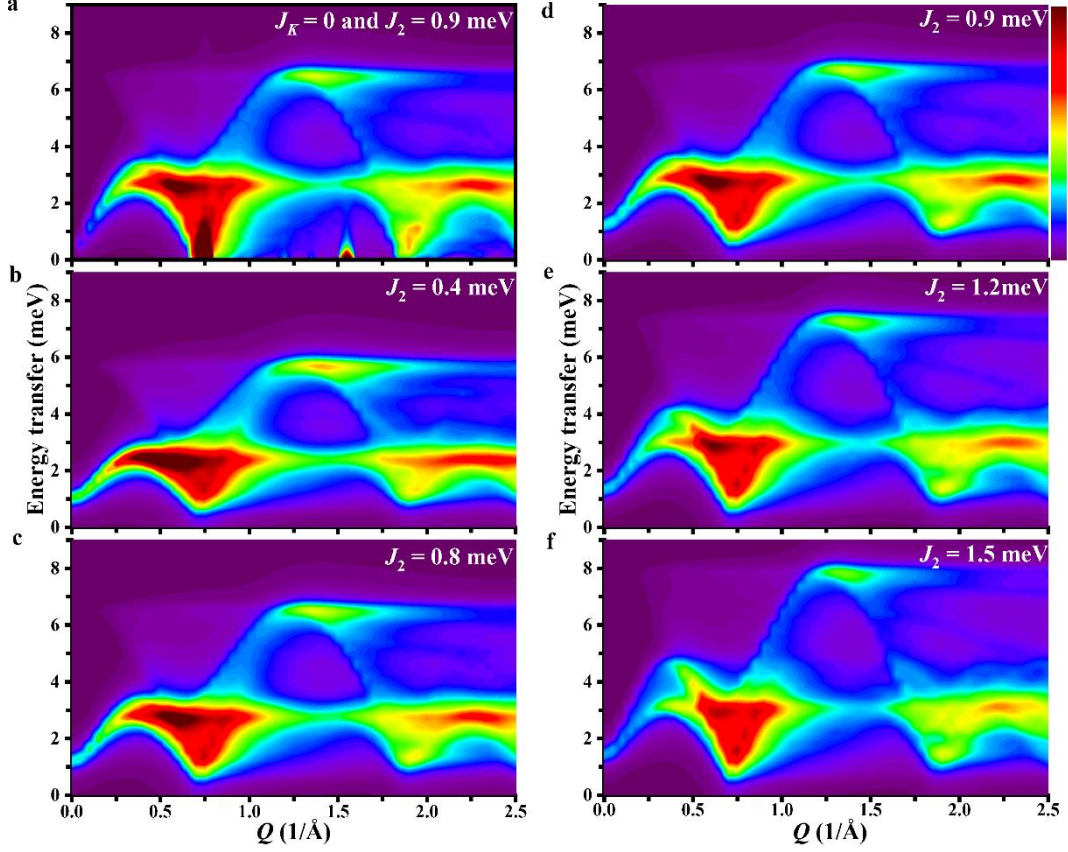
The pre-factors are due to the projection operator (i.e., only components transverse to  $\mathbf{q}$  contribute). The power-average is given by:

$$I(q, \omega) = \frac{1}{4\pi} \int d\cos\theta d\phi I(q, \theta, \phi, \omega). \quad \text{S(21)}$$

#### 4.5 Results for typical parameters



**Supplementary Figure 5: Calculated INS spectra.** LSWT calculations and corresponding powder averages with different parameters.



**Supplementary Figure 6: Calculated INS spectra.** LSWT calculations and corresponding powder averages. **a** The calculated spectrum for the parameters corresponding to  $(J_1, J_2, J_3, J_K) = (-1.6, 0.9, 1.6, 0)$  meV with a zigzag ground state. **b-f** The calculated spectrum for the constant parameters  $(J_1, J_3, J_K) = (-1.6, 1.6, -0.25)$  meV with different  $J_2$ .

#### 4.6 Transformation into the general form

The Hamiltonian connected with the spin at position  $\mathbf{S}_r$  reads,

$$\begin{aligned}
 H_i = & J_1 \sum_{k=1,2,3} \mathbf{S}_r \cdot \mathbf{S}_{r+\mathbf{n}_k} + I(\mathbf{S}_r \cdot \hat{c})(\mathbf{S}_{r+\mathbf{n}_k} \cdot \hat{c}) + J_K(\mathbf{S}_r \cdot \mathbf{n}_k)(\mathbf{S}_{r+\mathbf{n}_k} \cdot \mathbf{n}_k) \\
 & + \sum_{k=1,2,3} (J_\Gamma + J_D)(\mathbf{S}_r \cdot \hat{\varepsilon}_k)(\mathbf{S}_{r+\mathbf{n}_k} \cdot \hat{c}) + (J_\Gamma - J_D)(\mathbf{S}_{r+\mathbf{n}_k} \cdot \hat{\varepsilon}_k)(\mathbf{S}_r \cdot \hat{c})
 \end{aligned} \tag{S22}$$

Express the constant vector directly,

$$\begin{aligned}
 \hat{\mathbf{n}}_{\gamma_1} &= \frac{1}{\sqrt{2}}(\hat{i} - \hat{j}), & \hat{\mathbf{n}}_{\gamma_2} &= \frac{1}{\sqrt{2}}(\hat{j} - \hat{k}), & \hat{\mathbf{n}}_{\gamma_3} &= \frac{1}{\sqrt{2}}(\hat{k} - \hat{i}), \\
 \hat{\varepsilon}_{i,i+\gamma_1} &= \frac{1}{\sqrt{6}}(\hat{i} + \hat{j} - 2\hat{k}), & \hat{\varepsilon}_{i,i+\gamma_2} &= \frac{1}{\sqrt{6}}(-2\hat{i} + \hat{j} + \hat{k}), \\
 \hat{\varepsilon}_{i,i+\gamma_3} &= \frac{1}{\sqrt{6}}(\hat{i} - 2\hat{j} + \hat{k}), & \hat{c} &= \frac{1}{\sqrt{3}}(\hat{i} + \hat{j} + \hat{k})
 \end{aligned} \tag{S23}$$

and replace with them in S(21), then the Hamiltonian can be expressed as,

$$\begin{aligned}
H_i = & J_1 \sum_{k=1,2,3} \mathbf{S}_{r_i} \cdot \mathbf{S}_{r_i+\mathbf{n}_k} + \frac{I}{3} \sum_{k=1,2,3} \mathbf{S}_{r_i} \cdot \mathbf{S}_{r_i+\mathbf{n}_k} + \frac{I}{3} (S_{r_i}^x \cdot S_{r_i+\mathbf{n}_1}^y + S_{r_i}^y \cdot S_{r_i+\mathbf{n}_1}^x) \\
& + \frac{I}{3} (S_{r_i}^y \cdot S_{r_i+\mathbf{n}_2}^z + S_{r_i}^z \cdot S_{r_i+\mathbf{n}_2}^y) + \frac{I}{3} (S_{r_i}^x \cdot S_{r_i+\mathbf{n}_3}^z + S_{r_i}^z \cdot S_{r_i+\mathbf{n}_3}^x) \\
& + \frac{I}{3} (S_{r_i}^z \cdot S_{r_i+\mathbf{n}_1}^x + S_{r_i}^x \cdot S_{r_i+\mathbf{n}_1}^y + S_{r_i}^y \cdot S_{r_i+\mathbf{n}_1}^z + S_{r_i}^z \cdot S_{r_i+\mathbf{n}_1}^y) \\
& + \frac{I}{3} (S_{r_i}^x \cdot S_{r_i+\mathbf{n}_2}^y + S_{r_i}^y \cdot S_{r_i+\mathbf{n}_2}^z + S_{r_i}^z \cdot S_{r_i+\mathbf{n}_2}^x + S_{r_i}^x \cdot S_{r_i+\mathbf{n}_2}^z) \\
& + \frac{I}{3} (S_{r_i}^y \cdot S_{r_i+\mathbf{n}_3}^z + S_{r_i}^z \cdot S_{r_i+\mathbf{n}_3}^x + S_{r_i}^x \cdot S_{r_i+\mathbf{n}_3}^y + S_{r_i}^z \cdot S_{r_i+\mathbf{n}_3}^y) \\
& + \frac{J_K}{2} [(S_{r_i}^x - S_{r_i}^y)(S_{r_i+\mathbf{n}_1}^x - S_{r_i+\mathbf{n}_1}^y) + (S_{r_i}^y - S_{r_i}^z)(S_{r_i+\mathbf{n}_2}^y - S_{r_i+\mathbf{n}_2}^z) + (S_{r_i}^z - S_{r_i}^x)(S_{r_i+\mathbf{n}_3}^z - S_{r_i+\mathbf{n}_3}^x)] \\
& + \frac{J_\Gamma + J_D}{3\sqrt{2}} (S_{r_i}^x + S_{r_i}^y - 2S_{r_i}^z)(S_{r_i+\mathbf{n}_1}^x + S_{r_i+\mathbf{n}_1}^y + S_{r_i+\mathbf{n}_1}^z) + \frac{J_\Gamma - J_D}{3\sqrt{2}} [(S_{r_i}^x + S_{r_i}^y + S_{r_i}^z)(S_{r_i+\mathbf{n}_1}^x + S_{r_i+\mathbf{n}_1}^y - 2S_{r_i+\mathbf{n}_1}^z) \\
& + \frac{J_\Gamma + J_D}{3\sqrt{2}} (S_{r_i}^z + S_{r_i}^y - 2S_{r_i}^x)(S_{r_i+\mathbf{n}_2}^z + S_{r_i+\mathbf{n}_2}^y + S_{r_i+\mathbf{n}_2}^x) + \frac{J_\Gamma - J_D}{3\sqrt{2}} [(S_{r_i}^x + S_{r_i}^y + S_{r_i}^z)(S_{r_i+\mathbf{n}_2}^z + S_{r_i+\mathbf{n}_2}^y - 2S_{r_i+\mathbf{n}_2}^x) \\
& + \frac{J_\Gamma + J_D}{3\sqrt{2}} (S_{r_i}^z + S_{r_i}^x - 2S_{r_i}^y)(S_{r_i+\mathbf{n}_3}^z + S_{r_i+\mathbf{n}_3}^x + S_{r_i+\mathbf{n}_3}^y) + \frac{J_\Gamma - J_D}{3\sqrt{2}} [(S_{r_i}^x + S_{r_i}^y + S_{r_i}^z)(S_{r_i+\mathbf{n}_3}^z + S_{r_i+\mathbf{n}_3}^x - 2S_{r_i+\mathbf{n}_3}^y) \\
& = (J_1 + \frac{I}{3} + \frac{J_K}{2} + \frac{\sqrt{2}J_\Gamma}{3} \sum_{k=1,2,3} \mathbf{S}_{r_i} \cdot \mathbf{S}_{r_i+\mathbf{n}_k} - (\frac{J_K}{2} + \sqrt{2}J_\Gamma) \sum_{k=1,2,3} S_{r_i}^{\gamma_k} S_{r_i+\mathbf{n}_k}^{\gamma_k} \\
& + \sum_{k=1,2,3} (\frac{I}{3} + \frac{\sqrt{2}J_\Gamma}{3} - \frac{J_K}{2}) (S_{r_i}^{\alpha_k} S_{r_i+\mathbf{n}_k}^{\beta_k} + S_{r_i}^{\beta_k} S_{r_i+\mathbf{n}_k}^{\alpha_k}) \\
& + \frac{1}{3} (I - \frac{J_\Gamma}{\sqrt{2}}) \sum_{k=1,2,3} \sum_{\alpha_k \neq \gamma_k} (S_{r_i}^{\gamma_k} S_{r_i+\mathbf{n}_k}^{\alpha_k} + S_{r_i}^{\alpha_k} S_{r_i+\mathbf{n}_k}^{\gamma_k}) \\
& - \frac{J_D}{\sqrt{2}} \sum_{k=1,2,3} \sum_{\alpha_k \neq \gamma_k} (S_{r_i}^{\gamma_k} S_{r_i+\mathbf{n}_k}^{\alpha_k} - S_{r_i}^{\alpha_k} S_{r_i+\mathbf{n}_k}^{\gamma_k}), \tag{S(24)}
\end{aligned}$$

Where  $\gamma_k$  represents  $x, y, z$  corresponding to  $\mathbf{n}_1, \mathbf{n}_2, \mathbf{n}_3$  bond, respectively, and  $\alpha_k, \beta_k$  labels the other two components. Hence, there is a relationship between our model parameters and the parameters researchers generally use, that is,

$$\begin{aligned}
J &= J_1 + \frac{I}{3} + \frac{J_K}{2} + \frac{\sqrt{2}J_\Gamma}{3}, \\
K &= -(\frac{J_K}{2} + \sqrt{2}J_\Gamma), \\
\Gamma &= \frac{I}{3} + \frac{\sqrt{2}J_\Gamma}{3} - \frac{J_K}{2}, \\
\Gamma' &= \frac{1}{3} (I - \frac{J_\Gamma}{\sqrt{2}}) \tag{S(25)}
\end{aligned}$$

## Reference

- [1] H. Liu and G. Khaliullin, *Physical Review B* **97**, 014407 (2018).
- [2] R. Sano, Y. Kato, and Y. Motome, *Physical Review B* **97**, 014408 (2018).
- [3] P. Hofmann, *Solid State Physics: An Introduction* (Wiley-VCH, Deutsche Nationalbibliothek, 2015).
- [4] J. Chaloupka, G. Jackeli, and G. Khaliullin, *Phys Rev Lett* **105**, 027204 (2010).